Highlights

Flow induced vibration (FIV) of a pentagonal cylinder with high mass-damping ratio

Esmaeel Masoudi, Lian Gan, David Sims-Williams, Adam Marshall

- Flow induced vibration of a pentagonal cylinder with a high mass ratio is studied experimentally.
- VIV found to be dominant in most incidence angles for the pentagonal cylinder in low flow velocities.
- VIV in a pentagonal cylinder could be larger than a circular cylinder with a same mass ratio.
- Galloping is dominant in high incoming flow velocities and is maximum for incidences where VIV is negligible.

Flow induced vibration (FIV) of a pentagonal cylinder with high mass-damping ratio

Esmaeel Masoudi[a,b,*], Lian Gan[b,*], David Sims-Williams[b], Adam Marshall[b]

[a]*School of Civil, Aerospace and Design Engineering, University of Bristol, University Walk, Bristol, BS8 1TR, UK*
[b]*Department of Engineering, Durham University, Stockton Rd, Durham, DH1 3LE, UK*

Abstract

In this study, fluid structure interactions of a fixed and oscillating pentagonal cylinder are studied using experimental approaches. Specifically, flow induced vibration (FIV) of a pentagonal cylinder is studied with six different incidence angles (α) in a recirculating wind tunnel at fixed mass damping ratios. A series of free oscillation experiments are carried out in order to explore galloping behaviour as well as the lock-in region for vortex induced vibration (VIV). It is found that VIV for a pentagonal cylinder is substantially stronger than for a circular cylinder with a similar mass ratio. VIV maximum amplitude changes non-monotonically with incidence angle, and is smaller for incidences where galloping is dominant. Also, galloping was found to be substantially stronger where the stiffness of the system is lower.

Keywords: Pentagonal cylinders, Flow Induced Vibration (FIV), Galloping, Vortex Induced Vibration (VIV)

1. Introduction

Flow Induced Vibration (FIV) of various structures is of great interest in different kinds of engineering practices e.g, ocean, aerospace and civil engineering. This phenomena may cause destructive vibrations or on the other hand produce useful motions. Riser tubes on oil rigs in the middle of the ocean may vibrate due to oscillating waves or tidal currents. Airplane slender wings may flutter in certain speeds. Bridge structures may also experience galloping in case that the frequency of oscillation matches the natural frequency of the structure (Blevins, 1977). Tacomma Narrows bridge catastrophic incident was a result of destructive FIV on a bridge in result of high wind speeds (Billah and Scanlan, 1991). While the interest in FIV has historically been associated with preventing damage to structures, looking forward, it provides an opportunity for energy harvesting at a range of scales from the microscale through to tidal currents. These potential future applications make geometries which enhance FIV of new interest.

Nomenclature

α	Static incidence angle
α^*	Dimensionless static incidence angle
α_i^*	Dimensionless dynamic incidence angle
δ_0	Structural logarithmic decrement
δ_t	Total logarithmic decrement
Λ	Strouhal frequency energy content
ν	Kinematic viscosity of the fluid
ω_n	Angular natural frequency of the mass-spring system

*Corresponding authors
Email addresses: e.masoudi@bristol.ac.uk (Esmaeel Masoudi), lian.gan@durham.ac.uk (Lian Gan), d.b.sims-williams@durham.ac.uk (David Sims-Williams), adam.marshall@durham.ac.uk (Adam Marshall)

January 9, 2025

ω_v	Angular vibration frequency of the mass-spring system
ρ	Fluid density
ρ_s	Cylinder density
ζ	Damping coefficient with incoming flow velocity
ζ_0	Structural damping coefficient
ζ_t	Damping coefficient in still air $U_\infty = 0$
A^*	Dimensionless time averaged vibration amplitude
A_t^*	Dimensionless instantaneous vibration amplitude
A_{max}^*	Maximum dimensionless vibration amplitude
A_v	Vibration amplitude
C_L	Lift coefficient
c_m	Mechanical damping of the system
$C_{L,rms}$	Root-mean-square of the lift coefficient
D	Diameter of circular cylinder
D_i	Internal diameter of pentagonal cylinder
f^*	Frequency ratio $f^* = f_v/f_n$
f_n	Natural frequency of the mass-spring system
f_{St}	Strouhal frequency
f_v	Vibration frequency
k_s	Spring stiffness
m	Mass of cylinder
m^*	Mass ratio
$m^*\zeta_0$	Mass damping paramter
m_a	Added mass of cylinder
m_d	Displaced mass of cylinder
m_L	Mass of a cylinder per one meter length
$P(f)$	Power spectral density
S_G	Skop-Griffin parameter
t^*	Dimensionless time scale $t^* = tD/U_\infty$
U'_{hw}	Fluctuating component of U_{hw}
U^*	Reduced velocity
U_{hw}^{STD}	Standard deviation of U_{hw}
U_∞	Incoming flow velocity
U_{hw}	Flow velocity measured with hot wire anemometer
V_c	Volume of cylinder
OHR	Overheat ratio of hot wire anemometer
Re	Reynolds number
St	Strouhal number

Extensive research has been conducted on flow around a flexibly mounted circular cylinder (e.g., Bearman (1984); Blevins (1977); Sarpkaya (2004); Williamson and Govardhan (2004); Bearman (2011); Vandiver (2012)). Typically, studies in this field involve subjecting a flexibly mounted rigid circular cylinder to water or air flow. As the frequency of vortex shedding synchronizes with the system's natural frequency, an observable region of substantial amplitude oscillations, known as the lock-in region emerges. This phenomenon is known as Vortex-Induced Vibration (VIV) and was firstly found in a pioneering study by Feng (1968). Vibrations in VIV occur in limited range of the incident flow velocity and are mostly in a direction normal to the free stream velocity (Bearman, 1984).

However, research extends further to asymmetric shapes, where the structural symmetry is disrupted. In such cases, the incidence angle plays a pivotal role in determining the system's response. Beyond VIV-type responses, these systems may exhibit galloping or flutter type responses characterized by large amplitude oscillations at low frequencies (Parkinson and Smith (1964); Païdoussis et al. (2010)). Hartog (1932) was the first who proposed his criterion for galloping of ice-covered cables. Structures with square, rectangular, triangular, or D-shaped cross-sections, among

others, are particularly susceptible to galloping instability when asymmetry is introduced. Galloping and flutter are self-excited vibrations in the conventional sense that the vibration exciting force vanishes with the motion (Blevins, 1977). Flutter is an aerospace terminology for coupled torsion-plunge instability of airfoil structures, while galloping is the term favored by ocean and civil engineers for one degree of freedom instability of bluff structures in wind or ocean currents (Blevins, 1977). Galloping is driven by the instantaneous incidence angle between the body and the flow, $\beta = \tan^{-1}(\dot{y}/U_\infty)$, producing an asymmetric pressure distribution. Since the amplitude of the oscillation in galloping and flutter increases continuously with the flow velocity, they could be very catastrophic. A comprehensive review of investigations into galloping phenomena can be found in Païdoussis et al. (2010).

There are no systematic studies on FIVs of pentagonal cylinders, however other polygons such as equilateral triangular cylinders and square cylinders are widely studied in the literature (e.g. Parkinson and Smith (1964); Obasaju et al. (1990); Naudascher and Wang (1993); Deniz and Staubli (1997); Alonso et al. (2005); Su et al. (2007); Srigrarom and Koh (2008); Wang et al. (2011); Nemes et al. (2012); Alonso et al. (2012); Zhao et al. (2013); Alawadhi (2013); Tu et al. (2014); Zhao et al. (2014); Seyed-Aghazadeh et al. (2017); Li et al. (2019); Chen et al. (2020, 2023)). Parkinson and Smith (1964) showed the existence of galloping instability in a square cross-section at face orientation which corresponds to the case where the flat face of the square is placed perpendicular to the flow. Later on, in an experimental study Bokaian and Geoola (1984) discussed the existence of mixed modes of VIV and galloping in such structures. Obasaju et al. (1990) conducted an investigation into the flow over square cylinders at various angles of incidence while experiencing free oscillations in the streamwise direction. The study reported on amplitude-dependent vortex shedding modes and identified multiple sources of excitation. Wang and Zhou (2005) determined resonance modes for an elastic square cylinder with fixed supports across a wide velocity range. Nemes et al. (2012) examined the influence of incidence angle of a square section cylinder on the cylinder's FIV, where the direction of the vibration is transverse to the oncoming flow. Their amplitude response analysis showed that the transition between galloping and VIV occurs over a narrow range of angle of incidence. However, they reported that vortex shedding modes remain very similar to those found previously in VIV studies. Zhao et al. (2014) later however, doing more precise experiments for three distinct incidence angles, found a higher branch in FIV response of a square prism. They stated that this higher branch has caused by a sub-harmonic synchronization between the vortex shedding and the body oscillation frequency where two cycles of vortex shedding occur over one cycle of oscillation. A numerical study which allowed motion in both the transverse and streamwise directions, found a similar high-amplitude response regime (Zhao et al., 2013). Li et al. (2019) studied mode competition in the galloping of a square cylinder in laminar flow. They demonstrated that at large reduced velocities the wake vortices shed alternately at a relatively high frequency close to the vortex-shedding frequency of a stationary square cylinder, while the structure oscillates at a relatively low frequency close to the natural frequency of the structure.

While the FIV of a square prism have been extensively studied, less attention has been focused on the FIV of an equilateral triangular cylinder. Wang et al. (2014) numerically studied the FIV of a triangular prism at three different incidence angles i.e. $\alpha = 0, 30^\circ, 60^\circ$ where $\alpha = 0$ corresponds to corner orientation, where one of the corners is facing toward the flow, and $\alpha = 60^\circ$ to face orientation. They explained that at $\alpha = 0, 30^\circ$ VIV with small amplitude could be observed while at $\alpha = 60^\circ$ only galloping is observable. Using a fine increment, they found that the galloping response occurs when $\alpha > 40^\circ$. Zhang et al. (2016) experimentally studied the FIV of a triangular prism in face orientation. According to the variations of the amplitude and vibration frequency, they divided the responses into three different regions: VIV region, transition region and galloping region. In the transition region the vibration amplitude increases rapidly while the vibration frequency drops, deviating from the Strouhal number. Similar results were also reported in Ding et al. (2015). Seyed-Aghazadeh et al. (2017) carried out an experimental study of a flexibly mounted triangular prism with low mass ratio allowed to oscillate in the cross-flow direction, covering the entire range of incidence angles. They explained that for $\alpha < 30^\circ$ the prism does not oscillate but for larger values, two patterns in the response are observed and for values of $\alpha > 35^\circ$ the VIV-type and galloping type responses were connected with no separating distinct regions. Chen et al. (2020) using the immersed boundary method (IBM) studied the FIV of an equilateral triangular prism in various incidence angles. They found three different response regimes i.e. VIV dominated, galloping dominated and combined galloping/VIV response. They reported that in the VIV dominated regime, the vibration amplitude is approximately independent of incidence angle while in galloping regime the vibration amplitude monotonically increases with reduced velocity. Chen et al. (2023) numerically studied the effect of mass ratio (m^*) on VIV response of an equilateral triangular cylinder at Re= 200 using IBM. They explained that at $\alpha = 10^\circ$, VIV dominates and increasing m^* will result in the shrinkage of the large-amplitude

region, and lock-in moving to higher reduced velocities. At $\alpha = 40°$, the response varies with increasing mass ratio. The response types observed are combined VIV and galloping at $m^* = 2$, separated galloping at $m^* = 5$, and wavy galloping at $m^* = 10, 20$. Using Dynamic Mode Decomposition (DMD) analysis, they pointed out that the VIV vortex shedding mode and the galloping vortex shedding mode coexist with the scale of the galloping mode increasing with increasing amplitude while the VIV mode remains unaffected. In a recent study, Mousavisani et al. (2024) experimentally studied a flexible equilateral triangular cylinder allowed to oscillate in the cross-flow, inline and torsional direction in three different incidence angles $\alpha = 0, 30°, 60°$. They stated that in the corner orientation, both VIV and galloping could be observed in the response amplitude of the cylinder, however in face orientation, only galloping type responses are observed due to non-synchronised vortex shedding and oscillation frequency of the cylinder.

There are some studies on flow around stationary polygonal cylinders, including a pentagonal cylinder (Xu et al., 2017; Wang et al., 2020; Masoudi et al., 2021, 2023; Cheng et al., 2024). However, no specific study has delved into the FIV of these bluff bodies. To address this research gap, the current study is centered on exploring the FIV of a pentagonal cylinder (a polygon with side number $N = 5$) in wind tunnel facilities. For this purpose pneumatic probes as well as hot wire anemometers has been utilized to measure the flow in the wake of the cylinder. Initially, the experimental setup is detailed, allowing for the installation of both fixed and oscillating cylinders. Subsequently, preliminary results regarding the Strouhal numbers of the fixed cylinders are presented and compared with other numerical and experimental studies. Finally, the oscillatory behaviour of the pentagonal cylinder is investigated at various incidence angles and compared to a circular cylinder with a similar mass ratio. The present study focuses on cross-flow FIV only. In complex flow fields with two degrees of freedom systems, optimizing the natural frequency ratio between the two directions may either enhance or suppress vibration responses. Aligning one or both natural frequencies with the Strouhal frequency can amplify VIV, although the effect of the cross-flow natural frequency is typically more significant. Studies by Jauvtis and Williamson (2003, 2004) show that even at very low mass ratios, in-line oscillation has minimal impact on response branches, forces, and vortex wake modes.

2. Experimental setup and data collection

Most studies in the existing literature employ similar experimental setups to study VIV, typically utilising air bearings to minimise the damping coefficient (Vandiver, 2012). In contrast, here a novel system that deviates from the conventional approach is utilised by eliminating the use of bearing systems and associated mass. This alternative approach helps mitigate potential increases in system damping. Inspired by the Watt linkage system, a unique mass-spring system is designed for this purpose. The Watt linkage system, named after its inventor James Watt, is a linkage mechanism widely used in various engineering applications. It consists of a four-bar linkage mechanism composed of three interconnected bars or links with the fourth bar being the foundation that anchors the links. The design of the Watt linkage allows for linear motion, without reliance on any sliding elements. The proposed system allows adjustment of damping and stiffness, although it remains generally linear, with constant values for each test. Introducing nonlinear factors, such as variable stiffness or damping, could increase the system's adaptability to variable flow conditions and enhance energy harvesting efficiency (Vandiver, 2012; Garcia and Bernitsas, 2018; Zhang et al., 2024).

Figure 1 illustrates the the proposed mass-spring system as well as the definition of the incidence angle. The system incorporates three sets of carbon fiber squares arranged to form the mechanism consisting of a longitudinal leg positioned at the front and rear of the system, along with a transverse leg situated in the middle. The connection between these legs is achieved through the use of 0.5 mm thick spring steel flexures. These flexures are used for the pivots in order to eliminate friction in the system. The system is supported by a rectangular box made of an Item Aluminium extrusion measuring 40×40 mm, which serves as a sturdy framework and facilitates the connection of various components. To measure the movement of the cylinder during vibration, a Baumer laser displacement sensor with a response time of less than 10 ms and an accuracy of approximately ±0.2 mm is utilised. A small piece of rigid card is attached to the midpoint of the transverse leg, serving as the target for the laser beam. This card is positioned at a distance of 70 mm from the laser, which falls within the acceptable measurement range of the laser, spanning from 30 mm to 130 mm.

The system can be adjusted for stiffness by adding two springs. To facilitate the attachment of flexures to both the Items and legs, flexure adaptors are employed. To ensure smooth airflow over the model, a 10 mm thick acrylic

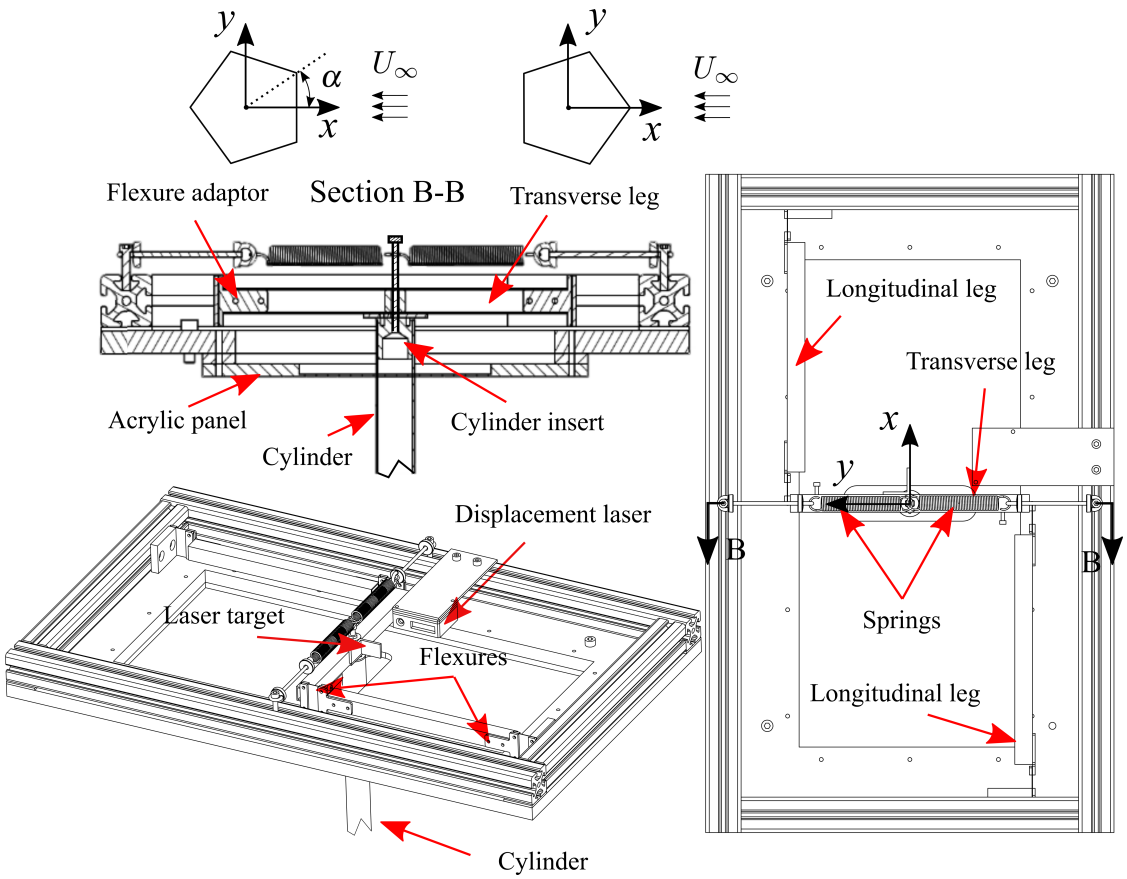

Figure 1: Schematic of the mass-spring experimental set up based on Watt linkage and the pentagonal cylinder indicating the incidence angle (α) definition.

panel is connected to the plywood with an additional 8 mm spacer. This configuration allows the internal side of the test section to be flush, promoting unhindered airflow. A slot is laser cut on the acrylic panel to allow for cylinder oscillation. However, this slot may contribute to air leakage into or from the test section. To prevent this air leakage, a transparent cover is specifically designed to fit onto the Item structure. The cover is assembled by utilising various laser-cut panels, which are securely glued together. Considering the significance of the cylinder's weight in FIV, carbon fibre was chosen as the material for manufacturing a pentagonal cylinder. Among the various methods for producing carbon fibre tubes, the prepreg carbon fibre lamination technique was selected to fabricate the cylinder in-house. The carbon fiber pentagonal cylinder with $D_i = 30$ mm then was cut to a length of 593 mm for assembly in the experimental setup. Note that D_i refers to the in-circle diameter of the pentagonal cylinder.

Additionally, a circular cylinder with similar diameter $D = 30$ mm is also supplied for testing alongside the pentagon. Note that considering the size of the wind tunnel test section, this leaves 1 mm gap between the cylinder and bottom of the test section. This falls in the gap recommended for VIV experiments (Williamson and Govardhan, 2004) which is $B_g = 0.04D$. The immersed length to diamter ratio for the cylinders is $L_s/D = 18.3$, which is similar to that in the work of Seyed-Aghazadeh et al. (2017) for a polygon with $N = 3$. Aluminum cylinder inserts, with dowel holes for incidence angle adjustment, were used to connect the cylinders to the transverse leg in the experimental setup (Figure 1). The angles on the insert for the pentagonal cylinder correspond to $\alpha^* = 0, 0.2, 0.4, 0.6, 0.8, 1$ at neutral position, where $\alpha^* = \alpha/36$. This enables comparison between the experimental findings and the numerical investigation of the fixed pentagonal cylinder presented in Masoudi et al. (2021, 2023). Note that for an oscillating polygon, the incidence angle is changing with the motion. The mass ratio of the cylinders are defined as

$$m^* = \frac{m}{m_d}, \tag{1}$$

where m is the mass of the cylinder plus other moving parts and $m_d = \rho \times V_c$ is the displaced mass of the cylinder, V_c is the volume of each cylinder and ρ is the density of air. Based on the designed experimental setup and the cylinders, the mass ratio m^* of the system is calculated as $m^* \approx 744$ for the pentagonal cylinder and $m^* \approx 741$ for the circular cylinder.

The experiments were carried out in the subsonic recirculating wind tunnel facilities at Durham university. The configuration of the wind tunnel involve a closed-circuit system utilising a belt-driven NICTORA Gebhardt centrifugal fan (ADH-k-1000) to generate fluid pressure. The fan is rated for a shaft input power of 30 kW with air intakes positioned on opposite sides of the fan. The tunnel includes a honeycomb and a screen in the plenum before contraction, aiding in achieving minimal flow angularity and high-quality flow uniformity within the test section. The nozzle features a contraction ratio of 7.1:1 over a length of 1.84 m. The test section within the tunnel measures 550 mm × 560 mm × 2440 mm in which the flow is capable of reaching speeds up to 45 m/s. The data is acquired using the National Instruments USB-6218 data acquisition system (DAQ).

The calibration process of devices and instruments used in this study included the calibration of pressure transducers, the 5-Hole probe, nozzle and the hot wire anemometer. Two sets of pressure transducers used which were responsible to measure the readings from the taps representing total and static pressure on the wind tunnel as well as the 5-Hole probe. These were calibrated using a manual liquid silicon based manometer. The nozzle then calibrated using a pitot-static tube positioned on the test section. The 5-Hole probe calibration is carried out in a dedicated calibration facility which consisted of a fan connected to a long diffuser and then a nozzle with a diameter of 102 mm and a traverse that rotates about two axes. A TSI Flow-Point 1500 constant temperature anemometer (CTA) unit is employed for hot wire measurements. While the 5-Hole probe mostly used for velocities of $U_\infty > 5$ m/s, the hot wire was used for measuring turbulence where the high frequency measurements are needed or lower velocities where the dynamic pressure is not high enough. The flow uniformity and angularity was measured using a 5-Hole probe. It was found that the flow exhibits minimal angularity ($\pm 1^\circ$) along the y-z plane and a consistent and uniform behaviour in the y direction within 1–4% of U_∞ across all examined heights. Furthermore, turbulent intensity of the airflow within the test section was measured using the hot wire anemometer and confirmed to be less than 0.5% in a wide range of incoming flow velocities in all locations.

3. Results and discussion

3.1. Strouhal number of the fixed cylinders

To facilitate the examination of the fixed cylinders, two blocks were manufactured and utilised in the experimental arrangement described in Section 2. These blocks were placed within the setup on the both sides of the transverse leg (see Figure 1) connecting the linkage to the Item. This configuration enables the secure fixation of the cylinder into position. The spacing between the hot wire probe head and the cylinder was established at $6D$. For the pentagonal cylinder the spacing was $6D_i$. It should be noted that the hot wire overheat ratio was OHR= 1.7 for all the tests. The free stream velocity was set to $U_\infty = 17.5$ m/s. This establishes the Reynolds number as 3.5×10^4. Note that Re= $U_\infty D/\nu$ for circular cylinder and Re= $U_\infty D_i/\nu$ for pentagonal cylinder, where ν is the kinematic viscosity of air. The z plane chosen for the measurements corresponds to the mid-span ($z = 0$).

Figure 2 (a,b) illustrates the velocity profile U_{hw}/U_∞ and the standard deviation of the velocity $U'_{hw} = U^{STD}_{hw}/U_\infty$ over the range $-4 \leq y/D \leq 4$. It should be noted that the measured velocity U_{hw} is dominated by x-component of the velocity u but is influenced by all three velocity components (u, v, w). The familiar bell-shaped velocity distribution behind the circular cylinders is clearly evident. Additionally, Figure 2 (b) reveals that the maximum unsteadiness occurs at $|y|/D \approx 0.6$. This indicates the location of the strongest vortex shedding in the y-direction, which, as observed here, should be symmetric for a circular cylinder. Figure 2 (c) demonstrates that the dominant Strouhal number within the range $0.4 \leq y/D \leq 3.8$ and $-3.8 \leq y/D \leq -0.4$ falls within the range of $0.2 \leq \mathrm{St} \leq 0.21$. These values align with those reported in the literature (Williamson, 1996; Xu et al., 2017). The Strouhal number is defined as St= $f_{st}D/U_\infty$ for the circular cylinder and St= $f_{st}D_i/U_\infty$ for the pentagonal cylinder. Here f_{st} is the vortex shedding frequency (or Strouhal frequency) based on U_{hw} signal. Figure 2 (d) illustrates the power density of the Fast Fourier

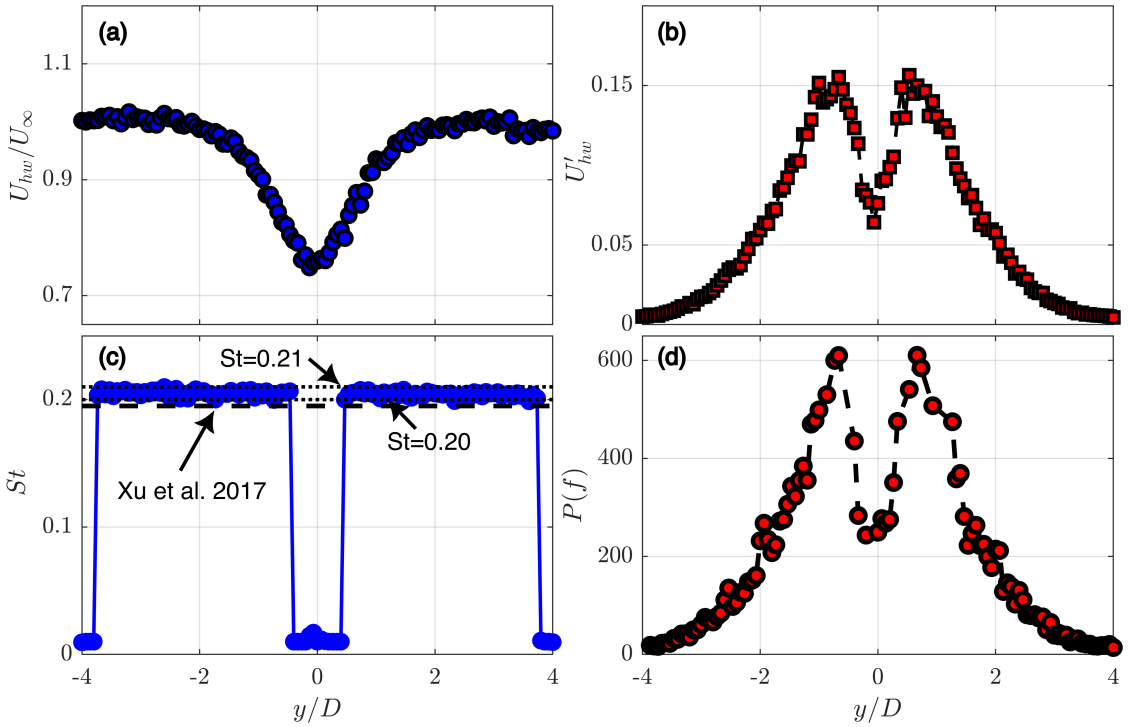

Figure 2: (a) Velocity profile (U_{hw}/U_∞), (b) the standard deviation of the velocity ($U'_{hw} = U^{STD}_{hw}/U_\infty$), (c) Strouhal number (St) and (d) the power of the frequency spectrum in the wake of the circular cylinder at Re= 3.5×10^4 measured over $-4 \leq y/D \leq 4$ and $z = 0$.

Transform (FFT) of the velocity signal (U_{hw}) at various y-positions. It is evident that the maximum power density occurs at approximately $|y|/D \approx 0.6$. This peak value corresponds to the y-coordinate where the vortex shedding is strongest, aligning well with Figure 2 (b).

Similar to the circular cylinder, the pentagonal cylinder is studied fixed into the setup. The aim was to investigate the Strouhal number on the fixed pentagonal cylinder at different incidence angles and various Reynolds numbers. For analysing the frequency of vortex shedding, the probe was fixed at $z = 0$, which corresponds to the mid-span, and $y/D_i = 1$, equivalent to $y = 30$ mm and $x/D_i = 6$. After completing the test for one incidence, the incidence angle on the pentagon was adjusted, and the setup was mounted again to conduct the same test with the new incidence angle. Incidences corresponding to $\alpha^* = 0 - 1$ with $\Delta\alpha^* = 0.2$ were tested, similar to the numerical study presented in Masoudi et al. (2023). Note that $\alpha^* = 0$ corresponds to corner orientation, while $\alpha^* = 1$ corresponds to face orientation. Figure 3 illustrates the results of these test series.

Firstly, it is evident that the Sts of $\alpha^* = 0.8$ and $\alpha^* = 1$ are substantially larger than other incidences. This aligns with findings of the numerical study of Masoudi et al. (2021). The discrepancy could be due to the behaviour of the separation points and the phenomena of the flapping motion. As described in Masoudi et al. (2021), the separated shear layers from the Primary Separation Points (PSP), reattach to the surface of the cylinder due to flapping motion of the separated shear layer and detach again from the downstream corner or Secondary Separation Point (SSP). In this context, PSP refers to the corner where the flow separate initially from the cylinder and SSP refers to the subsequent corner from which the flow separates from the cylinder for good. The SSP is the corner downstream of the PSP. This behaviour of the shear layer is reported for two cases of $\alpha^* = 0.8$ and $\alpha^* = 1$. This also leads to longer time-mean shear layer length and weak flapping motion amplitude (Masoudi et al., 2023). Also, as can be seen in Figure 3 (a) the St remains relatively constant and independent of Re for all α^*s. This behaviour occurs because the separation points are fixed on the corners of polygonal cylinders (Xu et al., 2017). In subcritical regimes, the variation in vortex shedding frequency is negligible for polygonal cylinders at their principal orientations (Xu et al., 2017). Figure 3 (a) confirms that this is the case for all other incidence angles for a pentagonal cylinder. Also includes the test results

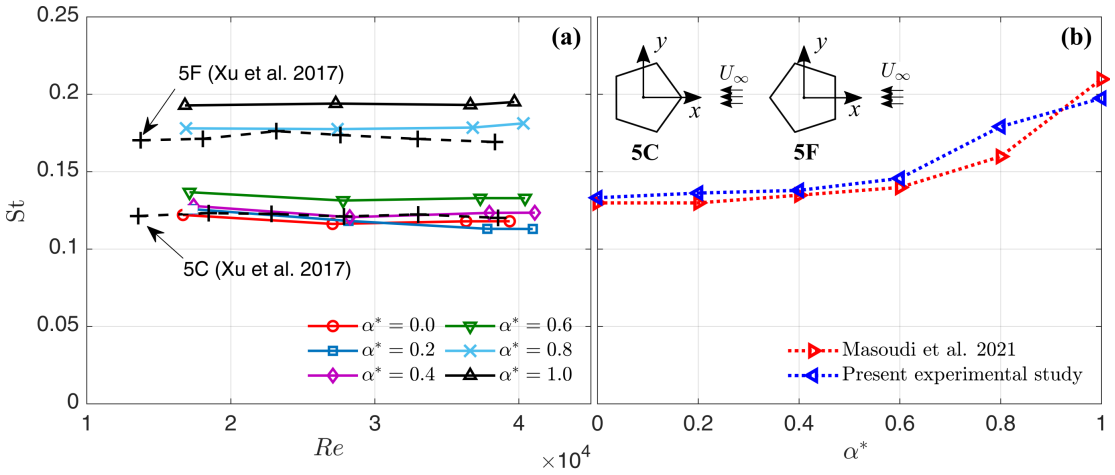

Figure 3: (a) Dependence of St on Re for the fixed pentagonal cylinder in various incidence angles. Also included the results from Xu et al. (2017) for the case of 5F (corresponding to $\alpha^* = 1$) and 5C (corresponding to $\alpha^* = 0$); and (b) St comparison between the present experimental study and numerical results from Masoudi et al. (2021) for the fixed pentagonal cylinder at Re= 10^4 for various incidence angles.

from Xu et al. (2017) for the 5F case (corresponding to $\alpha^* = 1$) and the 5C case (corresponding to $\alpha^* = 0$) of the fixed pentagonal cylinder. It is evident that the results for the 5C case are fairly comparable. However, for the 5F case, the St found here is slightly higher than those reported in Xu et al. (2017). This however match better with numerical results presented in Masoudi et al. (2021). To provide a more clear comparison between numerical and experimental findings, Figure 3 (b) is presented, focusing on Re= 10^4. As can be observed, the results exhibit a fairly comparable trend.

3.2. Free decay tests (pluck tests)

3.2.1. Tests with $U_\infty = 0$

The free decay test, also referred to as the pluck test, is a widely employed experimental technique to analyse the behaviour of a mass-spring systems in VIV studies. In this test, the system is initially displaced from its equilibrium position and then released to freely oscillate. The subsequent motion is recorded and analysed to determine important parameters such as the logarithmic decrement and damping coefficient. The logarithmic decrement δ is a measure of the rate at which the system's energy dissipates over time (Meirovitch, 2010). It is calculated by determining the natural logarithm of the amplitude ratio of two successive periods of the oscillations. A higher logarithmic decrement indicates stronger damping, showing that the system dissipates energy more rapidly, resulting in quicker damping of its oscillations. Conversely, a lower logarithmic decrement suggests less damping, indicating that the system's oscillations persist for a longer duration. The damping coefficient ζ, on the other hand, quantifies the amount of damping in the mass-spring system. It is typically determined using the logarithmic decrement and the known characteristics of the system, such as the mass and stiffness. By performing free decay tests and calculating the logarithmic decrement and damping coefficient, it is possible to determine the mass damping parameter $m^*\zeta$, which is a crucial and informative parameter for understanding the VIV of cylinders.

The system damping is obtained by measuring the logarithmic decrement δ_t, as the cylinder is vibrating in still air, and can be expressed as (Brika and Laneville, 1995)

$$\delta_t = \delta_A + \delta_B, \tag{2}$$

where δ_B is the base damping of the system which is independent of the vibration amplitude and δ_A is the portion of δ_t that is proportional to the square of the vibration amplitude. δ_B can be estimated from the recordings of the cylinder vibrating at small amplitudes. It is made up of the structural damping δ_0, and the aerodynamic viscous damping. For a circular cylinder, this can be written as (Sarpkaya, 1979)

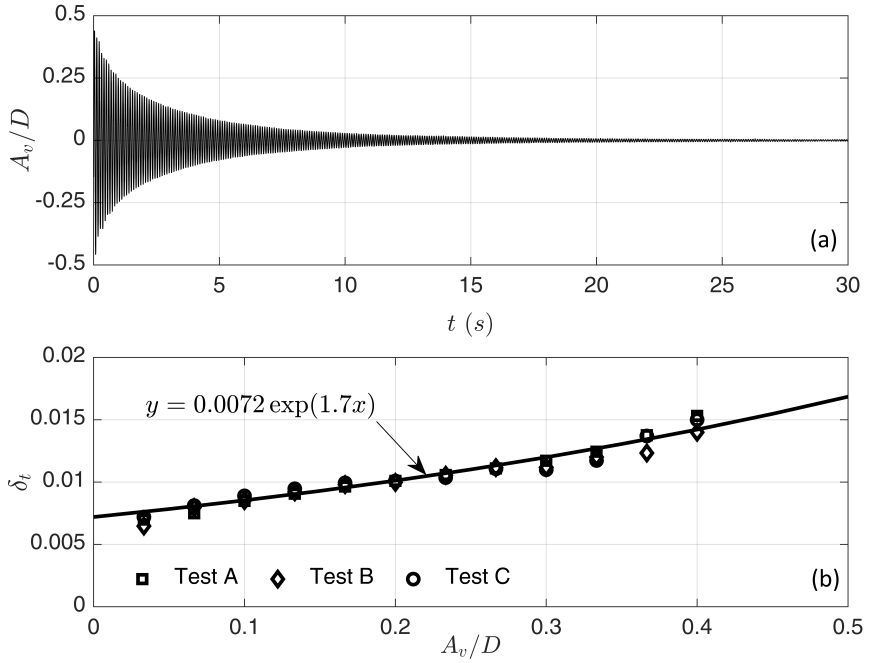

Figure 4: (a) The pluck test results sample for the circular cylinder at k_s = 2182 N/m and (b) the total logarithmic decrement *vs.* dimensionless vibration amplitude (A_v/D) for the circular cylinder corresponding to pluck tests with k_s = 2182 N/m.

$$\delta_B = \delta_0 + \frac{\rho}{\rho_s}\sqrt{\frac{32\nu}{\omega_n D^2}}\frac{\pi}{1-(d/D)^2}, \tag{3}$$

where $\omega_n = 2\pi f_n$, d = 27 mm is the internal diameter of the circular cylinder and ρ_s is the density of the circular cylinder that is $\rho_s = 4m_L/\pi(D^2 - d^2)$, where m_L = 0.194 kg/m is the mass per unit length of the circular cylinder. According to Sarpkaya (1979), structural damping (δ_0) may be determined by first vibrating the structure in still air, at a relatively high frequency (high k_s) and at very small amplitudes, so as to determine δ_B, and then subtracting the aerodynamic viscous damping through the use of equation 3. For evaluating δ_B, k_s = 2182 N/m is considered which corresponds to $f_n = 10.75 \pm 0.05$ Hz. The natural frequency of the system was evaluated to be $f_n = 3.85 \pm 0.05$ Hz for k_s = 220 N/m and $f_n = 8.75 \pm 0.05$ Hz for k_s = 1244 N/m. Figure 4 illustrates the sample test results for pluck test in still air of the circular cylinder with k_s = 2182 N/m and the corresponding δ_B. Note that as $A_v/D \to 0$, $\delta_t = \delta_B$. Hence, δ_B = 0.0072, determined by an arbitrary exponential fitting curve as illustrated in Figure 4. According to equation 3, the aerodynamic viscous damping for the circular cylinder is $\approx 1.2 \times 10^{-3}$ which accounts for $\approx$ 16.3% of δ_B. This means that the structural damping of the system is δ_0 = 0.006 and hence ζ_0 = 0.000955. This leads to $m^*\zeta_0$ = 0.7105 for the pentagonal cylinder and $m^*\zeta_0$ = 0.7076 for the circular cylinder. These values are larger than that used in studies on the square cylinder (Zhao et al., 2014) with $m^*\zeta_0$ = 0.0068 and the equilateral triangular cylinder (Seyed-Aghazadeh et al., 2017) with $m^*\zeta_0$ = 0.0526, both conducted in water tunnels. It is well established that lower $m^*\zeta_0$ results in a stronger VIV response in general (Khalak and Williamson, 1999; Williamson and Govardhan, 2004). A comprehensive list of VIV studies with corresponding $m^*\zeta_0$ values is available in Williamson and Govardhan (2004) and Masoudi (2024). It should be noted that the mechanical damping of the system, denoted as c_m and ζ are related as below (Nemes et al., 2012)

$$\zeta_0 = \frac{c_m}{2\sqrt{k_s(m+m_a)}} \tag{4}$$

where m and m_a are the mass and added mass of the cylinder respectively. Added mass usually considered to be near zero for cylinders oscillating in air. Therefore for the case shown in Figure 4, $c_m = 5.646 \times 10^{-4}$ N.s/m. System

damping for some electromagnetic devices, where damping arises from forces between levitated magnets and induced coil currents, can also be determined using the free decay test in principle, although specialized testing usually is necessary to obtain accurate damping coefficients (Pancharoen et al., 2017; Hasani and Rahaghi, 2022). In practice, environmental factors, for instance biofouling in ocean environment, and fairings could alter system damping and mass ratio, and consequently the structure natural frequency over time (Kiu et al., 2011; Yu et al., 2015; Xie et al., 2015; Jadidi and Zeinoddini, 2020).

3.2.2. Tests with $U_\infty > 0$

One way to identify possible energy input from the wind to the cylinders is to carry out pluck tests in incoming flow velocities, $U_\infty > 0$ and study its effect on damping coefficient. For carrying out pluck tests in flow for the circular cylinder, three different spring stiffness values were considered. Each of the cases involved ten distinct incoming flow velocities in a range of $0 < U_\infty \leq 3.5$ m/s corresponding to $f_{st}/f_n \leq 4$. Since the experiments were at low tunnel velocities, hot wire anemometer is more accurate than a pressure-based velocity measurement. U_∞ was measured at $y/D \approx 4$ and at $x/D = 6$ before giving the cylinder the initial incitation, while the vibration amplitude was recorded using the displacement sensor. Note that according to Figure 2, at $y/D \geq 2.5$, $U_{hw} \approx U_\infty$ for circular cylinder. For the pentagonal cylinder, based on Masoudi et al. (2021) and Wang et al. (2019), the wake width is at most approximately 1.3 times larger than that of the circular cylinder and therefore at $y/D \geq 3.5$, $U_{hw} \approx U_\infty$. The location of the probe head was also limited based on test section window arrangement and the traverse movability. Four pluck tests were conducted for each U_∞, and the average of measurements was considered as the final result. The standard deviation of the measurements was typically less than $O\,(1 \times 10^{-4})$ for ζ.

In contrast to conducting pluck tests in still air (where $U_\infty = 0$), pluck tests performed in flow may not result in the vibration amplitude reaching zero. To ensure a fair comparison of damping coefficients, two different methods were employed to calculate ζ. The first method involved calculating ζ within a range of vibration amplitudes A_v, while the second method involved calculating ζ within a range of cylinder vibration velocities ($A_v f_n/D$). This approach was taken to ensure that the conclusions drawn would hold true regardless of the chosen method for calculating ζ. Figure 5 illustrates the results. The solid lines represent the results obtained using the first method, with $0.04 \leq A_v/D \leq 0.4$, while the dashed line represents the results obtained using the second method, with $1 \leq A_v f_n/D \leq 4$. Figure 5 (a) shows the actual ζ values, while Figure 5 (b) displays $(\zeta - \zeta_t)/\zeta_t$ as a percentage value, where ζ_t represents the damping coefficient in still air (see equation 2). The horizontal axis in both graphs represents f_{st}/f_n, which is a well-established parameter in studying VIV (Sarpkaya, 2004).

The results depicted in Figure 5 (a) clearly indicate that as f_{st}/f_n approaches 1, the damping coefficient ζ reaches a minimum for all cases. This observation holds true regardless of the value of k_s or the method used to calculate ζ. Therefore, it can be concluded that irrespective of the occurrence of VIV on a cylinder, there is an energy input from the wind to the cylinder when f_{st}/f_n is approximately equal to 1. It is worth noting that the specific incoming flow velocity associated with this condition varies across different k_s cases. Additionally, the precise value of f_{st}/f_n at which ζ reaches its minimum is slightly above unity (around 1.1). This finding is consistent with numerous other studies on VIV (Sarpkaya, 2004; Williamson and Govardhan, 2004). Examining Figure 5 (b), it can be concluded that the data collapses reasonably well when plotted as $(\zeta - \zeta_t)/\zeta_t$. It becomes evident that the maximum reduction in ζ occurs for the case with $k_s = 1244$ N/m, which amounts to approximately -63%. This particular case also exhibits the lowest actual value of ζ according to Figure 5 (a). In terms of the reduction in ζ, the case with $k_s = 220$ N/m shows the smallest reduction. However, in terms of the absolute values of ζ, the case with $k_s = 2182$ N/m exhibits the highest values. The structural damping coefficient ζ_0 is illustrated in Figure 5 too. It is clear that only a few data points fall below ζ_0, suggesting the highest likelihood of VIV occurrence for those cases. This also suggests that even though the trends in both method (amplitude bound and vibration velocity bound) to calculate ζ are quite similar, using different methods could predict different conclusions for VIV occurrence.

The same set of experiments were also carried out for the pentagonal cylinder. According to the results for the case of the circular cylinder, it was decided to only do the experiments with $k_s = 1244$ N/m. Because this is the case that led to the lowest value of ζ and highest energy absorption from the flow (lowest $(\zeta - \zeta_t)/\zeta_t$). Also, since both methods of measuring ζ in Figure 5, had similar trends, it was decided to go ahead with the amplitude bound method for the pentagonal cylinder. For all of the incidences, a similar vibration amplitude bound of $0.4 \leq A_v/D_i \leq 0.9$ is considered for calculating ζ. It should be noted that the lower bound had to be large enough since in some cases, consistent vibrations were observed after carrying out the pluck tests. This generally leads to getting higher values

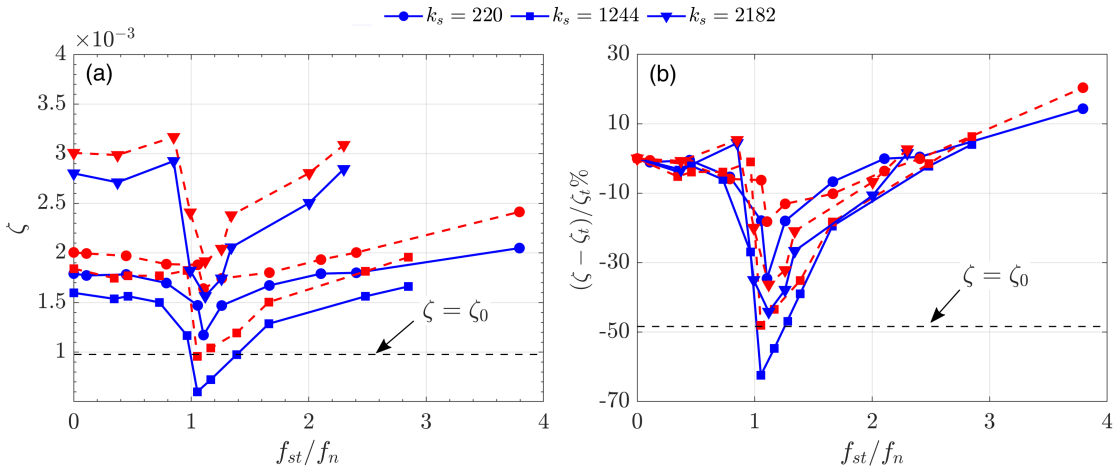

Figure 5: The pluck test results for the circular cylinder with incoming flow velocities of $0 < U_\infty \leq 3.5$ m/s presented as (a) damping coefficient ζ, and (b) the drop in damping coefficient compared to pluck tests in still air $(\zeta - \zeta_t)/\zeta_t$ %. Solid lines are results based on method 1 (amplitude bound: $0.04 \leq A_v/D \leq 0.4$) and the dashed lines are results based on method 2 (vibration velocity bound:$1 \leq A_v f_n/D \leq 4$) for calculating damping coefficient ζ. Three different spring stiffness are considered ($k_s = 220$ N/m, $k_s = 1244$ N/m and $k_s = 2182$ N/m).

for absolute ζ. Similar to the circular cylinder, ten different incoming flow velocities in a range of $0 < U_\infty < 5$ m/s corresponding to $f_{st}/f_n < 3$ were considered for each experiment case (incidence angle). On each velocity, four pluck tests were carried out and the average values of ζ and f_n were considered as the final results. Note that the incidence angle here, refer to the static incidence angle (when $A_v = 0$). The results are shown in Figure 6. Figure 6 (a) illustrates the pluck test vibration signal for $\alpha^* = 1$ (face orientation) at $U_\infty = 0.73$ m/s. This corresponds to Re$\approx$ 1500 and $f_{st}/f_n \approx 1.17$. The region for which ζ is calculated is plotted as red while it is clear that the vibration signal converge to a value of $A_v/D_i \approx 0.1$ after many oscillation cycles.

Observing Figure 6 (b,c), intriguing patterns emerge in the behaviour of the damping coefficient. Firstly, since these results are solely for $k_s = 1244$ N/m, the graphs depicted in (b) and (c) exhibit considerable similarity (opposite to Figure 5 (a,b)). Secondly, similar to the case of the circular cylinder (Figure 5), as f_{st}/f_n approaches 1 in $\alpha^* = 0, 0.2$, ζ declines. However, in other cases ($\alpha^* = 0.4 - 1$), ζ behaviour is more complex. In the case of $\alpha^* = 0.4$, ζ increases as f_{st}/f_n approaches 1. Nevertheless, it manifests negative $(\zeta - \zeta_t)/\zeta_t$ values for the majority of the examined cases. The behaviour of ζ for $\alpha^* = 0.6 - 1.0$ is notably similar. Initially, starting from zero velocity, there is a gradual decrease in ζ until approximately $f_{st}/f_n \approx 0.8$. Subsequently, ζ consistently increases with rising incoming flow velocities. The scenario with $\alpha^* = 1$ yields the lowest ζ values (among $\alpha^* = 0.6 - 1.0$) at $f_{st}/f_n = 1$, corresponding to an approximate 16% reduction in ζ compared to ζ_t. Evidently, among all scenarios, $\alpha^* = 0$ and $\alpha^* = 0.2$ display the most reduction in ζ at $f_{st}/f_n = 1$. For these scenarios, the $(\zeta - \zeta_t)/\zeta_t$ ratio reaches -57% and -48% respectively.

Given the relatively high lower bound of $A_v/D_i = 0.4$, the calculated damping ratio ζ in Figure 6 is predominantly influenced by aerodynamic damping components, especially δ_A, which changes dramatically with increasing vibration amplitude. Consequently, ζ values tend to be much higher compared to ζ_0. In summary, data presented in Figure 5 and Figure 6 demonstrate that when $f_{st}/f_n \to 1$, there is an energy input to the circular cylinder. For pentagonal cylinder there is an energy input from the air to the cylinder at $f_{st}/f_n \to 1$ for most cases but specially at $\alpha^* = 0, 0.2$.

3.3. Free oscillation tests

To conduct the free oscillating tests, a specific incoming flow velocity (U_∞) was set, and the cylinder was allowed to oscillate freely. Sufficient time was recorded for each case to ensure that the vibration had ample time to develop. In line with various other VIV studies, such as Brika and Laneville (1993), initial incitation was also applied to assess its impact on the results. In all cases, identical outcomes were obtained, leading to the conclusion that allowing enough time for the vibration to develop and stabilize yielded the same results as providing the cylinder with an initial incitation. The free oscillation tests were carried out for the pentagonal cylinder at six different initial incidence

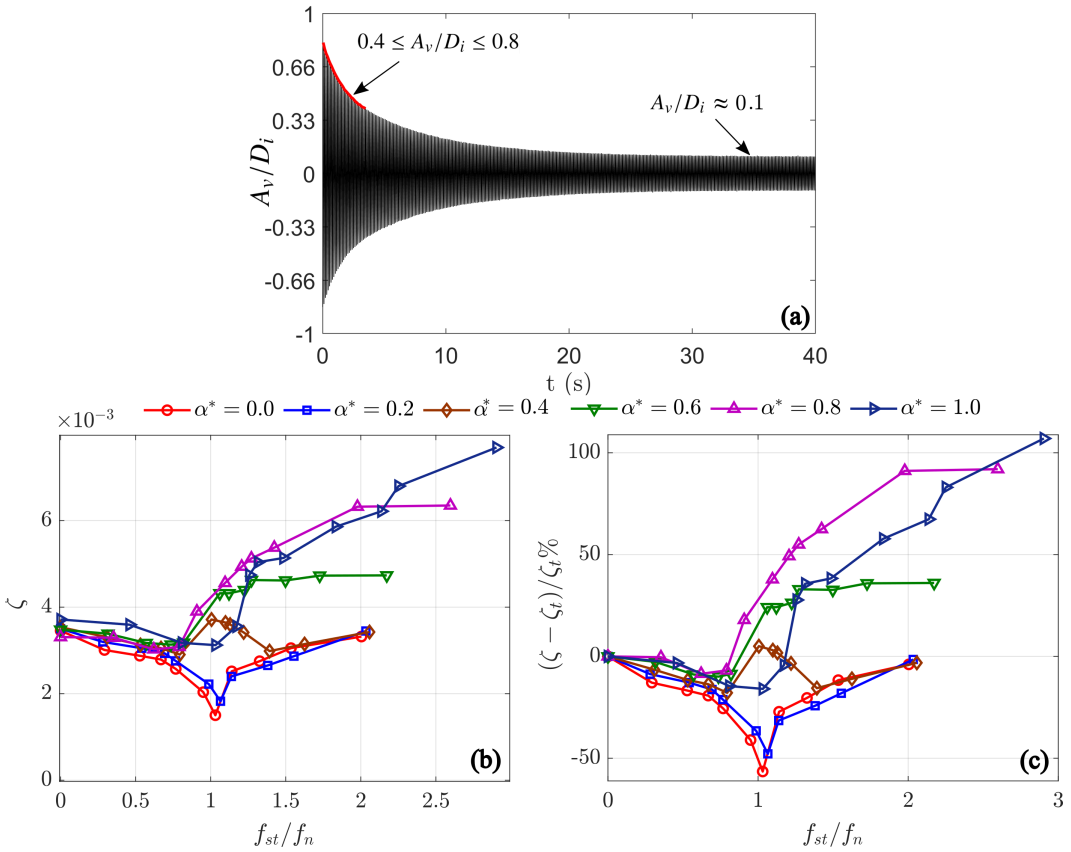

Figure 6: The pluck test results for the pentagonal cylinder at different incidence angles and with incoming flow velocities ($0 < U_\infty < 5$ m/s). (a) is the pluck test vibration signal for $\alpha^* = 1$ at $U_\infty = 0.7$ m/s, (b) is the damping coefficients ζ, and (c) is the drop in damping coefficient compared to pluck tests in still air $(\zeta - \zeta_t)/\zeta_t$ %. $k_s = 1244$ N/m and $0.4 \leq A_v/D_i \leq 0.8$ for calculating ζ.

angles and for the circular cylinder. The spring stiffness was set to $k_s = 1244$ N/m, consistent with the stiffness used in pluck tests with the flow. For each case, several values of U_∞ were considered to ensure that the tests adequately covered both the VIV and galloping regimes. The results of the free oscillation tests are presented in Figure 7, where $U^* = U_\infty/f_n D$ for the circular cylinder and $U^* = U_\infty/f_n D_i$ for the pentagonal cylinder. Note that Re varies in all tests with U^*, and the lock-in region (and its corresponding Re) is governed by f_n. For the circular cylinder with low $m^*\zeta$, Re has a significant effect (Bearman, 2011). The influence of Re on the circular cylinder with high $m^*\zeta$ and on polygonal cylinders requires further investigation.

The dimensionless amplitude is defined as $A^* = \overline{A_v}/D_i$ for the pentagonal cylinder and $A^* = \overline{A_v}/D$ for the circular cylinder with $\overline{A_v}$ being the averaged vibration amplitude in many vibrations cycles. Note that in galloping for the pentagonal cylinder, a mean value was observed in the vibration amplitude response in off-principal orientations, and was deducted from $\overline{A_v}$. The VIV and galloping regions (Blevins, 1977) can clearly be identified in Figure 7. In the following subsections VIV and galloping behaviour of the cases in Figure 7 are discussed.

3.3.1. VIV responses

The VIV response for the pentagonal cylinder in various initial incidence angles can be observed in Figure 7 at $U^* \approx 5 - 10$, which corresponds to $f_{st}/f_n \approx 1$ for St= $0.1 - 0.2$. Notably, the circular cylinder experiences VIV with a maximum amplitude of $A^*_{max} = 0.04$. This corresponds to $U^* = 6.41$, which aligns with $f_{st}/f_n = 1.04$. This A^*_{max} is significantly smaller than ones reported in other VIV studies conducted in wind tunnels (Feng, 1968; Brika and Laneville, 1995), probably due to higher $m^*\zeta_0$ used in this study. Moreover, as evident from the results, the circular cylinder does not experience galloping, which is not surprising. According to the definition of galloping, only non-

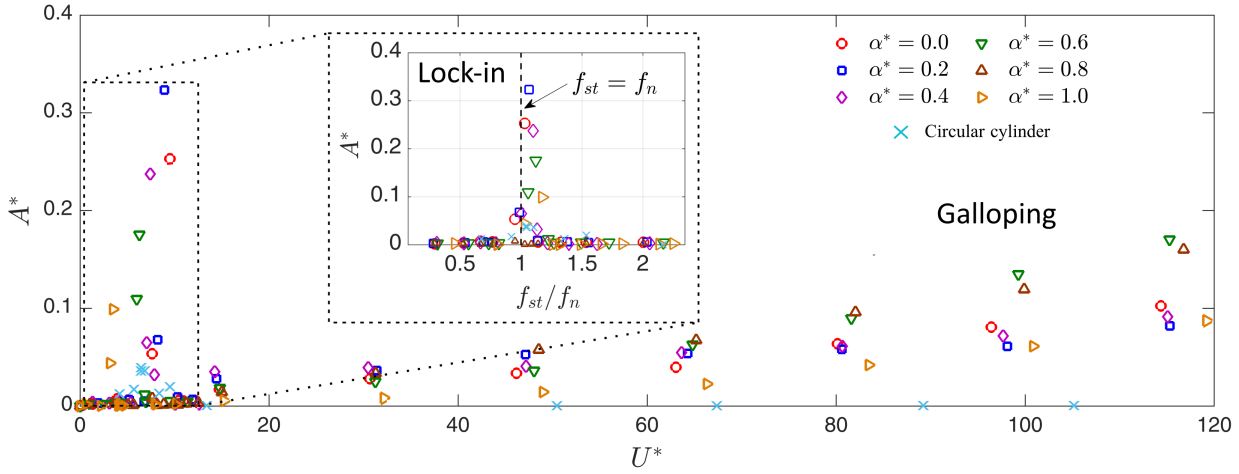

Figure 7: Free oscillating test results for the pentagonal cylinder ($m^*\zeta_0 = 0.7105$) as well as the circular cylinder ($m^*\zeta_0 = 0.7076$) at $k_s = 1244$ N/m in various incoming flow velocities ($0 < U_\infty < 35$ m/s)

circular cross sections are susceptible to this phenomenon (Païdoussis et al., 2011). Figure 7 also provides insight into the influence of initial incidence angles on VIV and galloping for a pentagon. The A^*_{max} values (VIV) for incidences ranging from $\alpha^* = 0$ to $\alpha^* = 1$ are 0.25, 0.32, 0.24, 0.17, 0.01, and 0.1, respectively. Notably, these values do not exhibit a monotonic relationship with respect to α^*. The corresponding U^* values for these peak values are 9.51, 8.94, 7.43, 6.27, 7.64, and 3.5, respectively. These values primarily align with the Strouhal frequencies, confirming that A^*_{max} occurs when $f_{st}/f_n \approx 1$. Figure 7 includes a zoomed in graph which provides a frequency domain representation of the results for the lock-in region. It is evident that the graphs converge around $f_{st}/f_n \approx 1$, indicating a collapse of the responses. It is clear that due to the limited resolution of the wind tunnel facility, only a few data points with high amplitude responses are available for each case. The width of the lock-in region appears narrow in all cases, potentially attributed to the relatively high $m^*\zeta_0$ of the system (Khalak and Williamson, 1997).

Upon comparing the FIV data presented in Figure 7 to Figure 6, one can observe a connection between the behaviour of VIV and the damping coefficient ζ. Firstly, the occurrences of A^*_{max} coincide with cases where ζ is minimal. The cases of $\alpha^* = 0$ and $\alpha^* = 0.2$ which had the lowest ζ and lowest $(\zeta - \zeta_t)/\zeta_t$, show the highest maximum VIV amplitude response. Additionally, the case of $\alpha^* = 0.8$, which exhibits the highest $(\zeta - \zeta_t)/\zeta_t$ for most f_{st}/f_n values, demonstrates negligible VIV response amplitudes. It is also noticeable that according to Figure 6, while $\alpha^* = 1$ exhibits lower ζ compared to $\alpha^* = 0.4$ and $\alpha^* = 0.6$, it possesses a smaller A^*_{max}. This could be due to using a large lower amplitude bound $A_v/D_i = 0.4$ for calculating ζ in Figure 6. In high vibration amplitudes, the δ_A term of the total damping (which is a function of incidence angle) is dominant (Equation 3) and therefore the energy input is not large enough to overcome it. Coming to lower vibration amplitudes δ_A falls dramatically, and the energy input to the cylinder is large enough to overcome the damping and hence larger vibration amplitude could be observed.

As described in section 3.2, the mass damping parameter for the circular cylinder is calculated as $m^*\zeta_0 = 0.7076$. This value surpasses the values reported by Feng (1968) as well as many other studies conducted in water channels. As described in Williamson and Govardhan (2004), the mass damping parameter plays a critical role in achieving high amplitude responses for VIV. Lower mass damping parameters result in higher amplitude responses, and vice versa, a relationship known as the Griffin plot. The Griffin plot is illustrated in Figure 8 (a). Here the Skop-Griffin parameter is defined as (Skop and Griffin, 1975)

$$S_G = 2\pi^3 \mathrm{St}^2 m^* \zeta_0 \tag{5}$$

The best fit for the Griffin plot is proposed by Sarpkaya (1978) as $A^*_{max} = C_1/\sqrt{C_2 + S_G^2}$ where $C_1 = 0.385$ and $C_2 = 0.120$. As it is clear in Figure 8 (a), this fit is not reliable in very low S_G values. Figure 8 (b) proposed by Williamson and Govardhan (2004) also demonstrate how data could collapse better (only in low S_G) by plotting

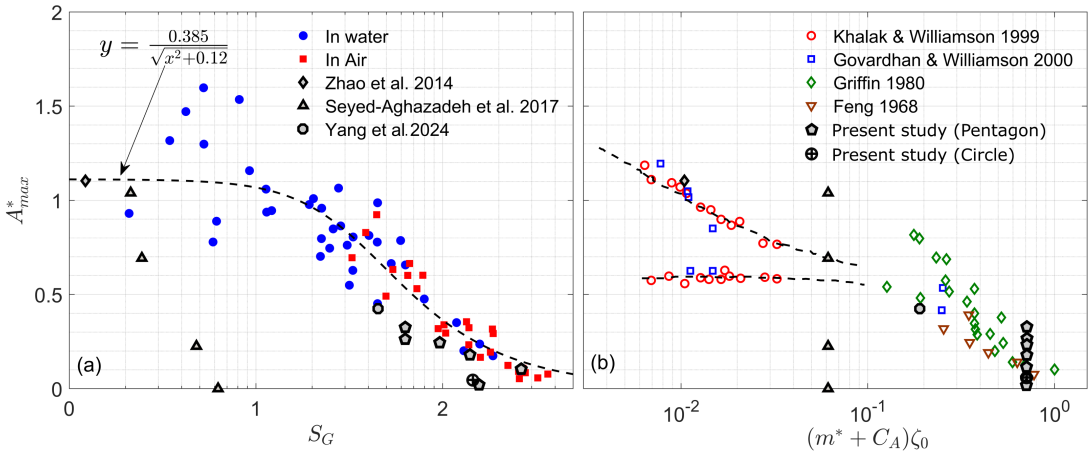

Figure 8: (a) The Griffin plot and (b) the mass damping parameter graph presented in Williamson and Govardhan (2004) both for maximum VIV response amplitude. The x-axis in both graphs are log scaled. The fitting relationship for the Griffin plot is adopted from Sarpkaya (1978). Also presented the data from Williamson and Govardhan (2004) for tests in water and air for various circular cylinders alongside the data from Khalak and Williamson (1999); Govardhan and Williamson (2000); Griffin (1980); Feng (1968) for circular cylinders with various $m^*\zeta_0$. Data from other studies concerning VIV in polygonal cylinders: Zhao et al. (2014) the case of $\alpha^* = 0$ (corner orientation) of a square cylinder; Seyed-Aghazadeh et al. (2017) the cases of $\alpha^* = 0, 0.16, 0.25, 0.33, 0.41, 0.5, 0.58$ for an equilateral triangular cylinder and Yang et al. (2024) for the the case of $\alpha^* = 0$ for a polygon with 18 sides. The results from this study are marked as ⬠ for the pentagonal cylinder and ⊕ for circular cylinder.

against $(m^* + C_A)\zeta_0$ where C_A is the potential added mass coefficient of the cylinder. In Figure 8 the results from this study is plotted alongside some other studies in literature on circular and polygonal cylinders. In Figure 8 (a) the data provided by Williamson and Govardhan (2004) are presented for tests carried out in water and air. In Figure 8 (b) the data presented by Khalak and Williamson (1999); Govardhan and Williamson (2000); Griffin (1980) and Feng (1968) pertains to circular cylinders under various mass-damping conditions. Additionally, Figure 8 depicts data from other studies concerning VIV in polygonal cylinders with different orientations. Specifically, from Zhao et al. (2014) results are for the case of $\alpha^* = 0$ (corner orientation) of a square cylinder, from Seyed-Aghazadeh et al. (2017) results are for the cases of $\alpha^* = 0, 0.16, 0.25, 0.33, 0.41, 0.5, 0.58$ for an equilateral triangular cylinder and from Yang et al. (2024) results are for the the case of $\alpha^* = 0$ for a polygon with 18 sides. Note that incidences presented from Zhao et al. (2014), Seyed-Aghazadeh et al. (2017) and Yang et al. (2024) are reported to be VIV dominated. The cases of $\alpha^* = 0, 0.16, 0.25, 0.33$ from Seyed-Aghazadeh et al. (2017) are corresponding to $A^* \approx 0$. Note that in Figure 8, D_i is used for polygons as the characteristic length in A^*_{max} and St, also all incidence angles were adjusted based on the definition in this study. The added mass coefficient for the triangular and square cylinders were considered as $C_A = 1.5, 1.4$ respectively (Zhao et al., 2014; Seyed-Aghazadeh et al., 2017) while for the other cases $C_A = 1$. For the cases in this study, since m^* is very high, C_A would only have a negligible effect.

While Figure 8 (b) approximately predicts the A^*_{max} of the circular cylinder presented here, Figure 8 (a) suggests that it is notably lower compared to other data points. Additionally, for the pentagon, while $\alpha^* = 0, 0.2, 0.4, 0.6, 1$ align reasonably well with the data points in Figure 8 (a), the case of $\alpha^* = 0.8$, characterized by minimal observed VIV, diverges significantly from the predicted values. It is evident that the Griffin plot and the mass-damping graph, originally intended for circular cylinders, and may not be suitable for evaluating VIV performance in polygons. For instance, Seyed-Aghazadeh et al. (2017) showed that in $\alpha^* = 0, 0.16, 0.25, 0.33$, no noticeable VIV can be observed for an equilateral triangular prism while $\log(S_G) < 1$ for these cases. Notably, the mass-damping graph (Figure 8 (b)) fails to consider cylinder orientation/Strouhal number effect. While such considerations may not be critical for circular cylinders, they are imperative for polygons like the pentagonal cylinder, where $m^*\zeta_0$ remains constant across all incidences despite vastly differing VIV behaviour.

According to Figure 7 it is remarkable that despite the high $m^*\zeta_0$ value, noticeable VIV responses were captured for the pentagonal cylinder, with A^*_{max} reaching as high as 0.3. Based on Figure 8 (b) for the pentagonal cylinder where $m^*\zeta_0 \approx 0.7$, the A^*_{max} should be approximately 0.06. This discrepancy can likely be attributed to differences in separation behaviour between polygonal and circular cylinders. In circular cylinders, flow separation occurs due

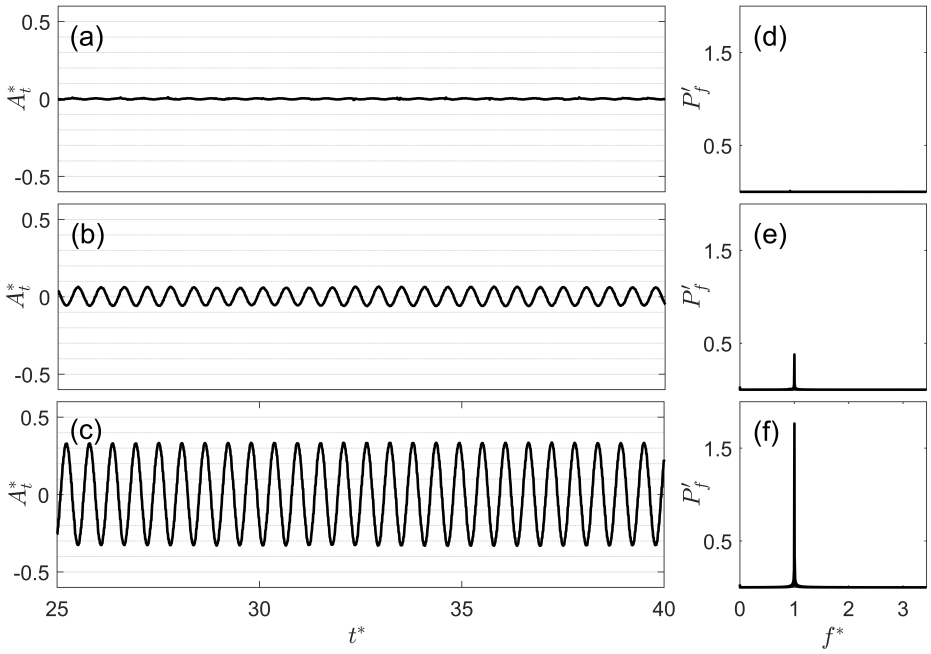

Figure 9: VIV signal for the pentagonal cylinder at $\alpha^* = 0.2$ in (a) $U^* = 4.5$, (b) $U^* = 8.2$ and (c) $U^* = 8.9$. The FFT power is illustrated for each case in (d,e,f). $P'_f = P_f \times 10^{-5}$, $f^* = f_v/f_n$ and $t^* = tD_i/U_\infty$

to the adverse pressure gradient when the surface is curved, leading to a negative velocity gradient on the surface. However, in polygonal cylinders with sharp corners (small enough N values), separation always occurs at the corners, and it seems that the separated boundary layer possesses greater strength Masoudi et al. (2021). This could explain the observed flapping motion in the separated shear layers of polygonal cylinders, while it is not commonly reported for circular cylinders (Masoudi et al., 2023). Stronger separated shear layers correspond to stronger vortex shedding, which, in turn, promotes the onset of VIV. Polygons (especially with low side numbers) however, undergo galloping which could interact with VIV in low U^* values. This means having stronger shear layer strength does not necessarily lead to higher VIV amplitudes.

Figure 9 depicts the VIV vibration amplitude for the pentagonal cylinder at $\alpha^* = 0.2$ for three different U^* values. The parameters P'_f and f^* are defined as $P'_f = P_f \times 10^{-5}$ and $f^* = f_v/f_n$, respectively. Here, P_f represents the FFT spectrum of the vibration signal, and f_v corresponds to the vibration frequency. In Figure 9 (a) and (d), where $U^* = 4.5$, no noticeable vibration is observed in the cylinder's behaviour, and there is no dominant frequency evident in the FFT spectrum of the signal. Moving on to Figure 9 (b) and (e), at $U^* = 8.2$, a small amplitude vibration is observed on the cylinder, resulting in the emergence of a dominant frequency. Subsequently, in Figure 9 (c) and (f), at $U^* = 8.9$, a large amplitude vibration is evident on the cylinder. Notably, the corresponding P_f value is significantly higher than that at $U^* = 8.2$, indicating a greater strength of vibration in this case. It is worth noting that in Figure 7, it was demonstrated that during large amplitude vibrations, $f_{st}/f_n \approx 1$. Similarly, in Figure 9, it is shown that this region also corresponds to $f^* = f_v/f_n \approx 1$. This alignment between frequencies is a typical observation in VIV studies, where the three frequencies (f_{st}, f_v, and f_n) exhibit synchronization (lock-in) with each other.

The incidence angle of the pentagonal cylinder is not constant during VIV. Development of VIV on the cylinder results in forming a cylinder velocity normal to the flow and therefore the resultant flow velocity is changing in magnitude and direction at each point of the vibration cycle. The VIV signal presented in Figure 9 can be expressed as $y = A_v \, sin\,(\omega_v t + \phi)$, in which $\omega_v = \omega_n$ is the vibration angular frequency and ϕ is the phase angle. Therefore, the cylinder velocity in reduced form can be expressed as $V^* = V/f_n D_i = A_v \omega_v \, cos\,(\omega_v t + \phi)\,/f_n D_i$. This then can be used to evaluate the instantaneous incidence angle as

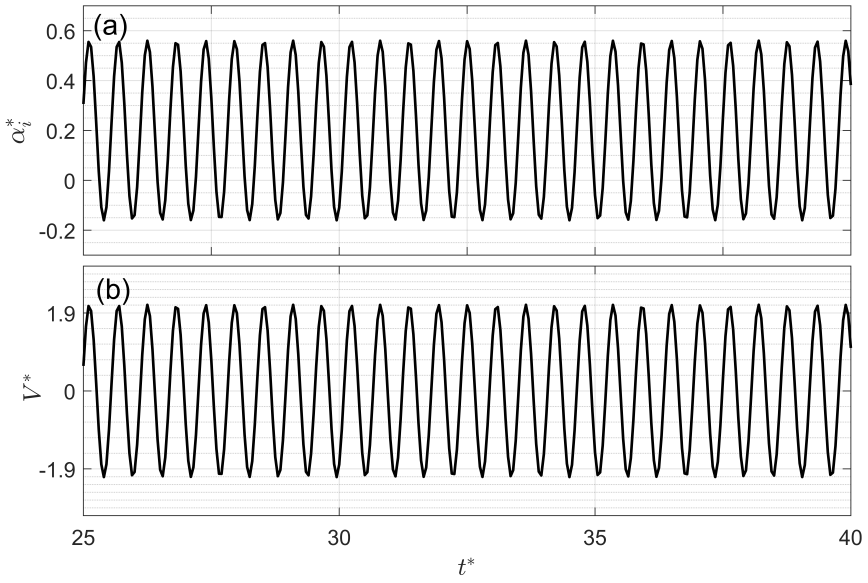

Figure 10: (a) Instantaneous incidence angle (α_i^*) and (b) reduced normal to flow velocity ($V^* = \overline{A_v}\omega_v cos(\omega_v t + \phi)/f_n D_i$) for the VIV signal of the pentagonal cylinder at $\alpha^* = 0.2$ when $U^* = 8.9$.

$$\alpha_i^* = \alpha^* + \frac{180}{\pi} tan^{-1}\left(\frac{V}{U_\infty}\right), \tag{6}$$

The instantaneous incidence angle for the pentagonal cylinder undergoing VIV at $\alpha^* = 0.2$ and $U^* = 8.9$, that is displayed in Figure 9 (c), is illustrated in Figure 10 (a). The cylinder velocity normal to the flow is also presented in Figure 10 (b). It is obvious that the α_i^* and V^* are in phase and both have $\pi/2$ phase difference to the vibration signal (Figure 9 (c)). When the cylinder is at its maximum amplitude $A_t^* = A_{max}^* \approx 0.33$, the $V^* \approx 0$ and $\alpha_i^* \approx 0.2$. Also, it can be seen that the average V^* is zero while the average α_i^* is $\alpha^* = 0.2$. Figure 10 is important since it determines how the incidence angle changes during vibration, which in turn gives information about the flow, considering flow around fixed cylinders. For the case presented in Figure 10, one can conclude that $0 \leq |\alpha_i^*| \leq 0.5$. According to Masoudi et al. (2023) the strength of the flapping motion of the separated shear layers is a monotonic function of α^* in pentagonal cylinders with maximum occurring for $\alpha^* = 0$. This in particular means that the cases with initial incidence angles of $0, 0.2$ in this study have instantaneous incidences in a range where flapping motion of the separated shear layer is generally high, and this could be the reason why these two cases have maximum VIV amplitude too. Conversely, evaluating α_i^* for the cases of $\alpha^* = 0.8, 1$ shows that α_i^* mostly falls in a range where the shear layer flapping motion is minimum and hence the maximum VIV amplitudes for these cases are small.

Figure 11 (a) illustrates the variation of various parameters with respect to the initial incidence angle for the pentagonal cylinder. A_{max}^* values are extracted from Figure 7, while the lift coefficient C_L and its root mean square ($C_{L,rms}$) for a fixed pentagonal cylinder are obtained from the numerical study of Masoudi et al. (2023). The theoretical value for A_{max}^* of a circular cylinder, $C_{L,rms}/2S_G$, is also plotted alongside other parameters using $C_{L,rms}$ and S_G of a pentagonal cylinder. It is evident that all parameters exhibit non-monotonic behaviour with respect to α^*. $C_{L,rms}/2S_G$ follows a similar trend to A_{max}^* and $C_{L,rms}$, reaching its maximum at $\alpha^* = 0.2$. At $\alpha^* = 0.8$ and $\alpha^* = 1$, the lowest values of $C_{L,rms}$ and $C_{L,rms}/2S_G$ are observed. This is reflected in the experiments, where these incidence angles correspond to the lowest A_{max}^*. The behaviour of $C_{L,rms}$ for $\alpha^* \geq 0.2$ is monotonic, while A_{max}^* experiences another increase at $\alpha^* = 1$. Considering previous studies on polygonal cylinders (Zhao et al., 2014; Seyed-Aghazadeh et al., 2017), it becomes evident that cases corresponding to face orientation ($\alpha^* = 1$) are consistently reported to be galloping dominated. Zhao et al. (2014) demonstrated that in some incidence angles for the square cylinder, vibrations at low U^* could be a combination of galloping and VIV. Having this in mind and assuming that the case of $\alpha^* = 1$ is galloping dominated, one can find better data correlation in the results, as depicted in Figure 11 (b). It is evident that

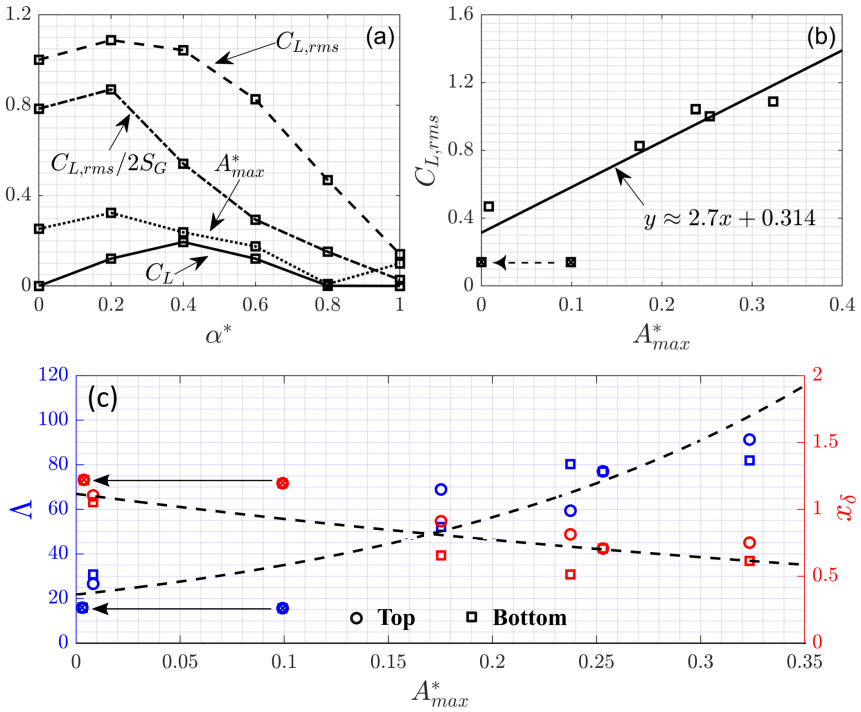

Figure 11: (a) The lift coefficient C_L and $C_{L,rms}$ for a fixed pentagonal cylinder, the present A^*_{max} and evaluated $C_{L,rms}/2S_G$ in various incidence angles α^* (b) the fitting relationship between $C_{L,rms}$ and A^*_{max} and (c) the fitting relationship between shear layer penetration length (x_δ) and flapping motion strength (Λ) for a fixed pentagonal cylinder with A^*_{max}. Data for fixed pentagonal cylinder are taken from numerical study on polygonal cylinders (Masoudi et al., 2023)

by assuming $A^*_{max} \approx 0$ for $\alpha^* = 1$, A^*_{max} could be calculated as follows:

$$A^*_{max} = \frac{C_{L,rms} - 0.314}{2.7}, \tag{7}$$

As explained above, the behaviour of vortex shedding and the separated shear layers could have direct impact on the VIV behaviour of the cylinder. Masoudi et al. (2023) showed that the separated shear layer strength for a pentagonal cylinder is maximum when $\alpha^* = 0, 0.2$. They also showed that the shear layer strength only drops dramatically when $\alpha^* = 0.8, 1$. While the α^* could change during VIV, it can be shown that for $\alpha^* = 0, 0.2$, the α^*_i envelope mostly stays in a range corresponding to high seperated shear layer strength (see Figure10). Stronger vortex shedding should result in higher fluctuations in lift and therefore higher forces on the cylinder. This could result to higher VIV amplitudes. To examine this, Figure 11 (c) is illustrated. Here, x_δ is the shear layer penetration distance which can be calculated by choosing a vorticity threshold ($\omega_z D_i/U = 3$) in the time averaged spanwise vorticity field of a fixed cylinder. Also, Λ is the shear layer flapping motion strength quantified by the energy content of the spectrum peak $X(f_d)$ where $X(f)$ is the energy spectrum (arbitrary unit) of fluctuating streamwise velocity component $u'(t)$ as below

$$\Lambda = \frac{1}{U_\infty} \int_{f_d - \Delta f}^{f_d + \Delta f} X(f_d)\, \mathrm{d}f, \tag{8}$$

where $\Delta f D_i/U_\infty = 0.02$. Both x_δ and Λ are taken from the numerical study on fixed polygons (Masoudi et al., 2023). It is clear from Figure 11 (c) that increasing Λ results in an exponential increase in A^*_{max} while increasing x_δ results in lowering the A^*_{max}. The data collapse better with the arbitrary fitting functions assuming that the case of $\alpha^* = 1$ is galloping dominated and $A^*_{max} \approx 0$. Figure 11 (c) simply states that having shorter separated shear layers results in more energy content in the flapping motion and that results in higher A^*_{max}. Figure 12 shows the space-time contours

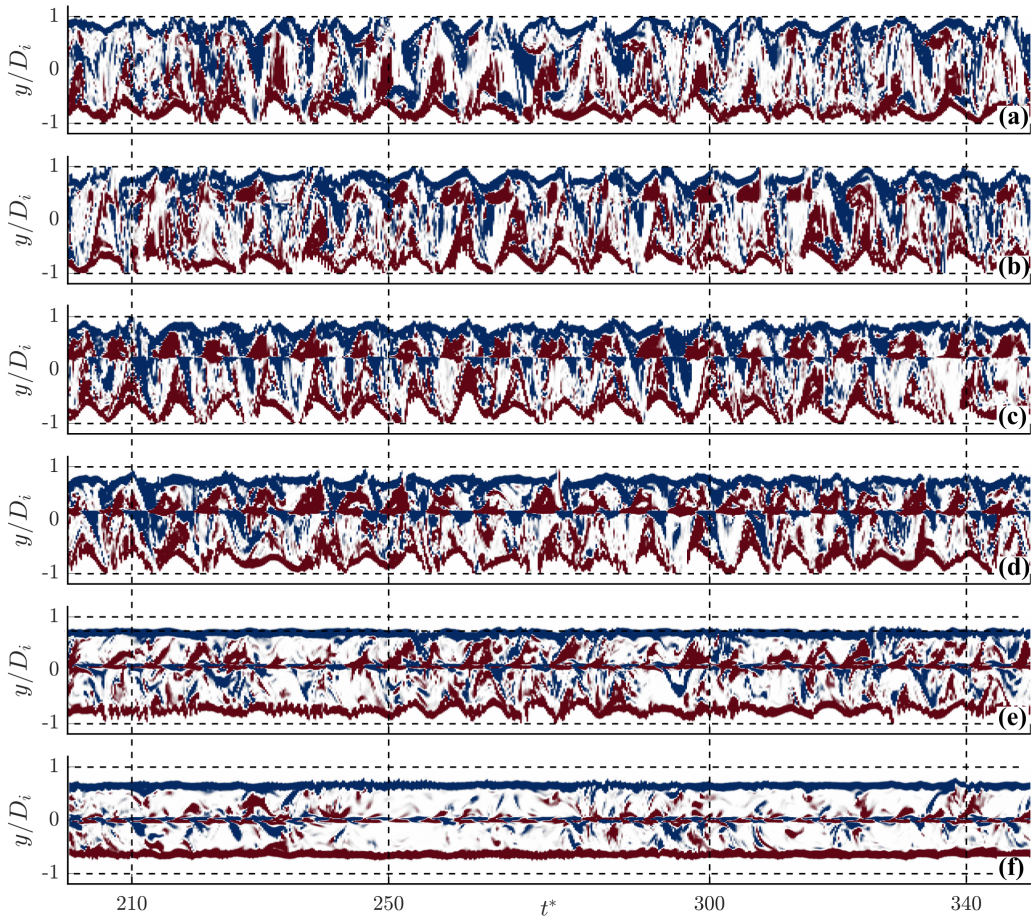

Figure 12: Space-time contours of the dimensionless spanwise vorticity $\omega_z D_i/U$ at $x = 0.6D_i$ and $-1 \leq y/D_i \leq 1$ for a fixed pentagonal cylinder at mid-span. Here (a-f) corresponds to $\alpha^* = 0, 0.2, 0.4, 0.6, 0.8, 1$ respectively. Data for fixed pentagonal cylinder are taken from numerical study on polygonal cylinders (Masoudi et al., 2023)

of the mid-span vorticity $\omega_z D_i/U$ for a fixed pentagonal cylinder at $\alpha^* = 0 - 1$ corresponding to (a-f) respectively. Data is sampled temporally over the range after the wake is fully developed, and spatially over $-1 \leq y/D_i \leq 1$, and at $x = 0.6D_i$, the streamwise distance before vortices roll up and detach from the shear layer in a time mean sense for all cases (Masoudi et al., 2021). For the case of $\alpha^* = 0.2$ undergoing VIV at $U^* = 8.9$ (see Figure 9), $0 \leq \alpha_i^* \leq 0.5$ as shown in Figure 10. Here in Figure 12 it can be seen that the separated shear layer has highest fluctuations in these cases for the fixed pentagonal cylinder. Figure 12 also shows that the amplitude of the shear layer flapping motion decreases as α^* increases with minimum amplitude for $\alpha^* = 0.8$ and $\alpha^* = 1$. This could justify why the cases of $\alpha^* = 0.8, 1$ exhibit the lowest maximum VIV amplitudes. These cases have more stable shear layers with less flapping motion of the separated shear layer as shown in Figure 12 (e,f).

3.3.2. Galloping responses

By examining the galloping responses in Figure 7, it becomes evident that the amplitude response exhibits a linear relationship with respect to U^*. However, the gradients of these lines are relatively small, generally ≤ 0.002. This could be attributed to the high mass damping ratio of the system. Moreover, it is noticeable that the gradients of the lines are quite similar, with only slight variations among different incidences. In most tested velocities, the symmetric cases of $\alpha^* = 1$ and $\alpha^* = 0$ demonstrate the lowest galloping amplitudes. The slope of the galloping response is comparatively larger for $\alpha^* = 0.8$ and $\alpha^* = 0.6$. It is generally expected to observe higher galloping amplitudes for

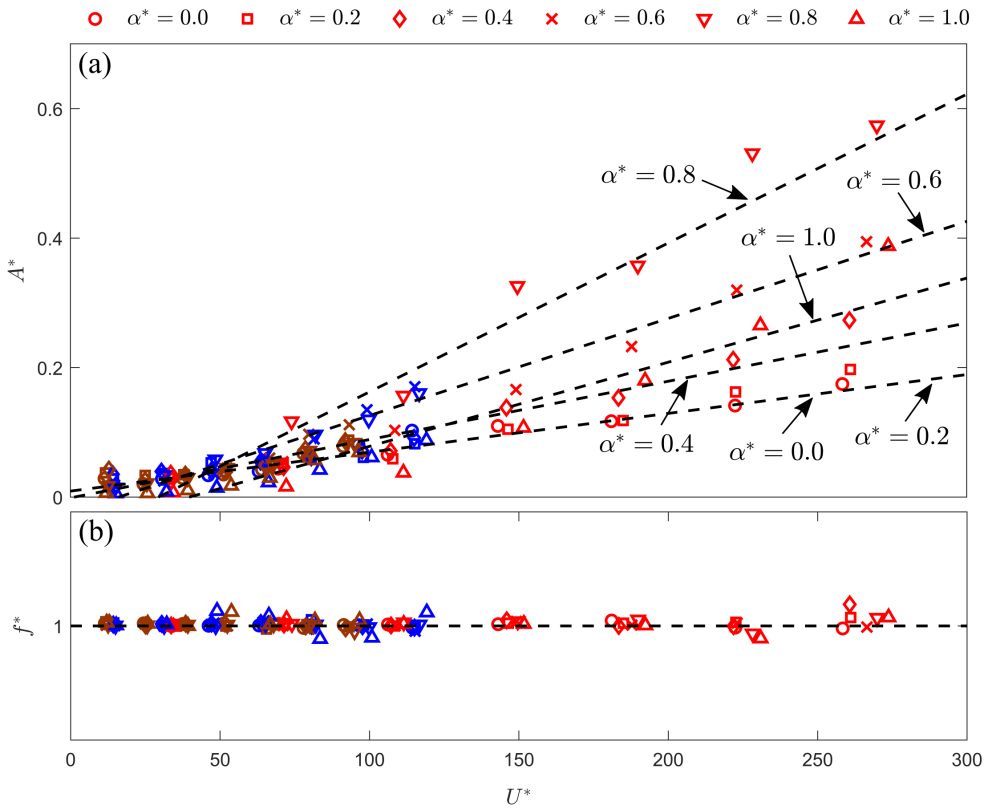

Figure 13: (a) Galloping response amplitude A^* for the pentagonal cylinder in various incidence angles and spring stiffness and (b) the corresponding frequency ratio $f^* = f_v/f_n$. Red, blue and brown markers correspond to k_s = 220 N/m, k_s = 1244 N/m and k_s = 2182 N/m.

asymmetric cases compared to symmetric cases, since the asymmetry in the cross-section allows for the generation of unbalanced fluid forces, promoting the galloping.

The galloping response of the pentagonal cylinder can be further examined by varying the spring stiffness. Figure 13 illustrates the galloping response amplitude A^* for the pentagonal cylinder at different incidence angles and corresponding frequency ratios $f^* = f_v/f_n$. Three different spring stiffness values are used for each incidence angle, represented by the red (k_s = 220 N/m), blue (k_s = 1244 N/m), and brown (k_s = 2182 N/m) markers in Figure 13. The closest linear fit for each incidence angle is also demonstrated in this Figure. It is evident that decreasing the spring stiffness results in larger galloping response amplitudes. This can be attributed to the weaker restoring force provided by the spring. With a lower spring stiffness, the lift force from the fluid flow can more easily overcome the weakened restoring force, leading to larger amplitude oscillations. This observation is consistent with the understanding that a weaker spring allows for a greater displacement of the structure and a more pronounced fluid-structure interaction.

Similar to Figure 7, it can be observed that the incidence angle $\alpha^* = 0.8$ exhibits the highest galloping responses, while $\alpha^* = 0$ and $\alpha^* = 0.2$ show the lowest responses. Previous research by Nemes et al. (2012) indicates that for a square cylinder, galloping becomes dominant for incidence angles $\alpha^* > 0.8$, with no VIV observed even at very low U^* values. In the case of a pentagonal cylinder in this study, a similar trend is observed for $\alpha^* = 0.8$, where no VIV is noticeable. However, in contrast to a square cylinder, the behaviour for the pentagonal cylinder is non-monotonic, with VIV dominating at $\alpha^* = 1$. It is however, shown in Section 3.3.1 that the VIV data collapse better with data from fixed cylinders if the VIV amplitude for $\alpha^* = 1$ is zero. Furthermore, Figure 13 (b) reveals that, similar to VIV, the frequency ratio f^* for galloping is approximately equal to 1. This observation aligns with previous studies (Bearman et al., 1987; Parkinson, 1989), confirming that $f^* \approx 1$ for galloping. It is important to note that unlike VIV, f_{st}/f_n is not unity. The galloping amplitude increases linearly with increasing flow velocity, and the slope of this relationship

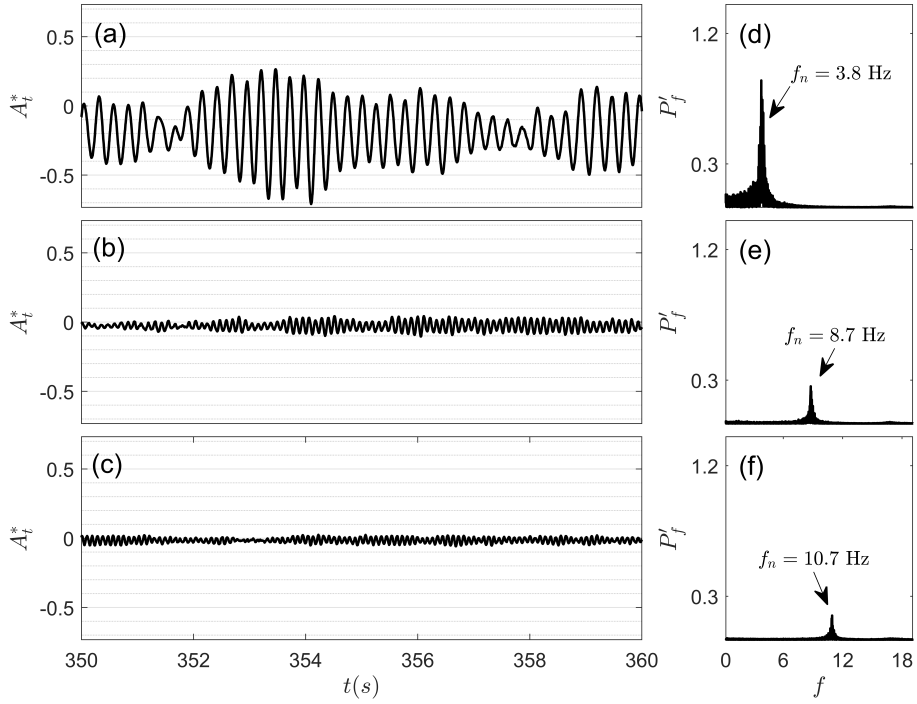

Figure 14: Galloping signal for the pentagonal cylinder at $\alpha^* = 0.2$ where $U_\infty = 25.5$ m/s (a) $k_s = 220$ N/m, (b) $k_s = 1244$ N/m and (c) $k_s = 2182$ N/m. The FFT power is illustrated on the left for each case in (d,e,f). $P_f' = P_f \times 10^{-5}$.

depends on the cross-section geometry, mass damping parameter, and spring stiffness.

Figure 14 depicts the galloping vibration amplitude for the pentagonal cylinder and $\alpha^* = 0.2$ at three different U^* values. The incoming flow velocity for all the cases is $U_\infty = 25.5$ m/s. The spring stiffness are (a) $k_s = 220$ N/m, (b) $k_s = 1244$ N/m and (c) $k_s = 2182$ N/m. One noticeable difference between Figure 14 and Figure 9 is the shape of the signal. In Figure 9, the signal appears clean with minimal noise or response overshoot. Conversely, in Figure 14, the signal demonstrates a higher level of noise with significant variation in A_t^*. This difference can be attributed to the nature of VIV, which typically occurs at lower velocities with lower turbulence levels. In galloping, the vortex shedding frequency f_{st} moves in and out of phase with the vibration frequency f_v, which can result in variation in A_t^*.

Another observation, particularly evident in Figure 14 (a), is that during galloping, the signal exhibits a non-zero mean value. This is a result of the asymmetric cross-section of the polygon in this orientation, which causes a non-zero lift to be applied to the cylinder. The mean value approaches zero as the spring stiffness increases, as seen in Figure 14 (b) and (c). Additionally, Figure 14 demonstrates how increasing the spring stiffness (k_s) leads to a decrease in the galloping response amplitude (while increasing the vibration frequency). This behaviour can be understood as a consequence of the stronger restoring force provided by the stiffer spring, which resists the displacement caused by the fluid forces and reduces the amplitude of the galloping motion. On the right-hand side of the signals in Figure 14 (d), (e), and (f), the corresponding vibration frequencies are illustrated. These vibration frequencies align with the natural frequency of the system. However, as the signal weakens due to the increased spring stiffness (k_s), the FFT power decreases, which is not surprising.

4. Conclusions

This study presents experimental investigations into vortex-induced vibration (VIV) and galloping phenomena in oscillating cylinders, specifically the circular cylinder and the pentagonal cylinder both having a mass damping parameter of $m^*\zeta_0 \approx 0.7$. A low-damping mass-spring system was designed to capture these phenomena in the

transverse (cross-flow) direction within a recirculating wind tunnel. The following conclusions can be drawn from this study:

- Firstly, Strouhal numbers was determined for flow around the circular cylinder and the pentagonal cylinder at six incidence angles, both in fixed position. Results are found to be consistent with previous experimental and numerical studies.
- The pluck tests with incoming flow velocity $U_\infty > 0$ showed complex behaviour. It was observed that at U_∞ corresponding to $f_{st}/f_n \approx 1$, a drop in the value of the damping coefficient (ζ) is noticed, indicating energy input from the airflow to the mass-spring system. For the circular cylinder, this drop was most significant when the spring stiffness was 1244 N/m compared to other stiffness values tested in this study (220 N/m and 2182 N/m). For the pentagonal cylinder, the pluck tests resulted in ζ drop in some incidences at U_∞ corresponding to $f_{st}/f_n \approx 1$, while in other cases, an increase in ζ was observed.
- In free oscillation tests, it was found that the circular cylinder exhibited VIV with the maximum amplitude $A^*_{max} = 0.04$, consistent with the predicted value based on the mass damping plot. For the pentagonal cylinder, both VIV and galloping were observed for most incidence angles, with VIV amplitude reaching up to $A^*_{max} = 0.33$ in some cases. This highlights the potential of using the pentagonal cylinder as an option to harvest flow energy.
- The galloping behaviour of the pentagonal cylinder was also investigated for various spring stiffness values, k_s. As expected, galloping amplitude increased as the k_s value decreased. Additionally, the dominant frequency in the galloping spectrum matched the natural frequency of the system in all cases, while the Strouhal frequency was generally much larger than both. This behaviour contrasts with VIV, where the Strouhal frequency f_{st}, natural frequency f_n, and vibration frequency f_v align.
- The vibration signals in galloping mode exhibited higher noise levels, likely due to more turbulence at higher flow velocities or to the asynchronous interaction of vibration frequency with vortex shedding frequency. VIV signals remained relatively clean.

References

E. M. Alawadhi. Numerical simulation of fluid flow past an oscillating triangular cylinder in a channel. *Journal of fluids engineering*, 135(4): 041202, 2013.

G. Alonso, J. Meseguer, and I. Pérez-Grande. Galloping instabilities of two-dimensional triangular cross-section bodies. *Experiments in Fluids*, 38:789–795, 2005.

G. Alonso, A. Sanz-Lobera, and J. Meseguer. Hysteresis phenomena in transverse galloping of triangular cross-section bodies. *Journal of Fluids and Structures*, 33:243–251, 2012.

P. Bearman. Circular cylinder wakes and vortex-induced vibrations. *Journal of Fluids and Structures*, 27(5-6):648–658, 2011.

P. Bearman, I. Gartshore, D. Maull, and G. Parkinson. Experiments on flow-induced vibration of a square-section cylinder. *Journal of Fluids and Structures*, 1(1):19–34, 1987.

P. W. Bearman. Vortex shedding from oscillating bluff bodies. *Annual review of fluid mechanics*, 16(1):195–222, 1984.

K. Y. Billah and R. H. Scanlan. Resonance, tacoma narrows bridge failure, and undergraduate physics textbooks. *American Journal of Physics*, 59 (2):118–124, 1991.

R. D. Blevins. Flow-induced vibration. *New York, Van Nostrand Reinhold Co., 1977. 377 p.*, 1977.

A. Bokaian and F. Geoola. Hydroelastic instabilities of square cylinders. *Journal of Sound and Vibration*, 92(1):117 – 141, 1984.

D. Brika and A. Laneville. Vortex-induced vibrations of a long flexible circular cylinder. *Journal of Fluid Mechanics*, 250:481–508, 1993.

D. Brika and A. Laneville. An experimental study of the aeolian vibrations of a flexible circular cylinder at different incidences. *Journal of Fluids and Structures*, 9(4):371–391, 1995.

W. Chen, C. Ji, D. Xu, Z. Zhang, and Y. Wei. Flow-induced vibrations of an equilateral triangular prism at various angles of attack. *Journal of Fluids and Structures*, 97:103099, 2020.

W. Chen, Y. Wei, C. Ji, and Y. Zhao. Mass ratio effects on flow-induced vibrations of an equilateral triangular prism. *Journal of Fluids and Structures*, 116:103808, 2023.

H. Cheng, E. Masoudi, Y. Liu, and L. Gan. On the asymmetric vortex evolution in the near wake behind polygonal cylinders in an incident flow. *Ocean Engineering*, 307:118142, 2024.

S. Deniz and T. Staubli. Oscillating rectangular and octagonal profiles: interaction of leading-and trailing-edge vortex formation. *Journal of Fluids and Structures*, 11(1):3–31, 1997.

L. Ding, L. Zhang, C. Wu, X. Mao, and D. Jiang. Flow induced motion and energy harvesting of bluff bodies with different cross sections. *Energy Conversion and Management*, 91:416–426, 2015.

C. Feng. The measurement of vortex induced effects in flow past stationary and oscillating circular and d-section cylinders. Master's thesis, University of British Columbia, 1968.
E. M. Garcia and M. M. Bernitsas. Effect of damping on variable added mass and lift of circular cylinders in vortex-induced vibrations. *Journal of Fluids and Structures*, 80:451–472, 2018.
R. Govardhan and C. Williamson. Modes of vortex formation and frequency response of a freely vibrating cylinder. *Journal of Fluid Mechanics*, 420:85–130, 2000.
O. Griffin. Vortex-excited cross-flow vibrations of a single cylindrical tube. *Pressure Vessel Technology*, 1980.
D. Hartog. Transmission line vibration due to sleet. *Transactions of the American Institute of Electrical Engineers*, 51(4):1074–1076, Dec 1932.
M. Hasani and M. I. Rahaghi. The optimization of an electromagnetic vibration energy harvester based on developed electromagnetic damping models. *Energy Conversion and Management*, 254:115271, 2022.
P. Jadidi and M. Zeinoddini. Influence of hard marine fouling on energy harvesting from vortex-induced vibrations of a single-cylinder. *Renewable energy*, 152:516–528, 2020.
N. Jauvtis and C. Williamson. Vortex-induced vibration of a cylinder with two degrees of freedom. *Journal of fluids and structures*, 17(7): 1035–1042, 2003.
N. a. Jauvtis and C. Williamson. The effect of two degrees of freedom on vortex-induced vibration at low mass and damping. *Journal of Fluid Mechanics*, 509:23–62, 2004.
A. Khalak and C. Williamson. Fluid forces and dynamics of a hydroelastic structure with very low mass and damping. *Journal of Fluids and Structures*, 11(8):973–982, 1997.
A. Khalak and C. H. Williamson. Motions, forces and mode transitions in vortex-induced vibrations at low mass-damping. *Journal of fluids and Structures*, 13(7-8):813–851, 1999.
K. Kiu, B. Stappenbelt, and K. Thiagarajan. Effects of uniform surface roughness on vortex-induced vibration of towed vertical cylinders. *Journal of Sound and Vibration*, 330(20):4753–4763, 2011.
X. Li, Z. Lyu, J. Kou, and W. Zhang. Mode competition in galloping of a square cylinder at low reynolds number. *Journal of Fluid Mechanics*, 867:516–555, 2019.
E. Masoudi. *Flow around stationary and oscillating polygonal cylinders*. PhD thesis, Durham University, 2024.
E. Masoudi, L. Gan, and D. Sims-Williams. Large eddy simulation of incident flows around polygonal cylinders. *Physics of Fluids*, 33(10):105112, 2021.
E. Masoudi, D. Sims-Williams, and L. Gan. Flow separation from polygonal cylinders in an incident flow. *Physical Review Fluids*, 8(1):014701, 2023.
L. Meirovitch. *Fundamentals of vibrations*. Waveland Press, 2010.
S. Mousavisani, H. Samandari, and B. Seyed-Aghazadeh. Experimental investigation of flow-induced vibration and flow field characteristics of a flexible triangular cylinder. *Journal of Fluid Mechanics*, 979:A15, 2024.
E. Naudascher and Y. Wang. Flow-induced vibrations of prismatic bodies and grids of prisms. *Journal of Fluids and Structures*, 7(4):341–373, 1993.
A. Nemes, J. Zhao, D. L. Jacono, and J. Sheridan. The interaction between flow-induced vibration mechanisms of a square cylinder with varying angles of attack. *Journal of Fluid Mechanics*, 710:102–130, 2012.
E. Obasaju, R. Ermshaus, and E. Naudascher. Vortex-induced streamwise oscillations of a square-section cylinder in a uniform stream. *Journal of Fluid Mechanics*, 213:171–189, 1990.
M. P. Païdoussis, S. J. Price, and E. De Langre. *Fluid-structure interactions: cross-flow-induced instabilities*. Cambridge University Press, 2010.
M. P. Païdoussis, S. J. Price, and E. De Langre. *Fluid-structure interactions: cross-flow-induced instabilities*. Cambridge University Press, 2011.
K. Pancharoen, D. Zhu, and S. Beeby. Temperature dependence of a magnetically levitated electromagnetic vibration energy harvester. *Sensors and Actuators A: Physical*, 256:1–11, 2017.
G. Parkinson. Phenomena and modelling of flow-induced vibrations of bluff bodies. *Progress in Aerospace Sciences*, 26(2):169–224, 1989.
G. V. Parkinson and J. D. Smith. The square prism as an aeroelastic nonlinear oscillator. *The Quarterly Journal of Mechanics and Applied Mathematics*, 17(2):225–239, 05 1964.
T. Sarpkaya. Fluid forces on oscillating cylinders. *Nasa Sti/recon Technical Report A*, 78:275–290, 1978.
T. Sarpkaya. Vortex-induced oscillations: A selective review. *Journal of Applied Mechanics*, 46(2):241–258, 06 1979.
T. Sarpkaya. A critical review of the intrinsic nature of vortex-induced vibrations. *Journal of fluids and structures*, 19(4):389–447, 2004.
B. Seyed-Aghazadeh, D. W. Carlson, and Y. Modarres-Sadeghi. Vortex-induced vibration and galloping of prisms with triangular cross-sections. *Journal of Fluid Mechanics*, 817:590–618, 2017.
R. Skop and O. Griffin. On a theory for the vortex-excited oscillations of flexible cylindrical structures. *Journal of Sound and Vibration*, 41(3): 263–274, 1975.
S. Srigrarom and A. Koh. Flow field of self-excited rotationally oscillating equilateral triangular cylinder. *Journal of fluids and structures*, 24(5): 750–755, 2008.
Z. Su, Y. Liu, H. Zhang, and D. Zhang. Numerical simulation of vortex-induced vibration of a square cylinder. *Journal of mechanical science and technology*, 21:1415–1424, 2007.
J. Tu, D. Zhou, Y. Bao, Z. Han, and R. Li. Flow characteristics and flow-induced forces of a stationary and rotating triangular cylinder with different incidence angles at low reynolds numbers. *Journal of Fluids and Structures*, 45:107 – 123, 2014. ISSN 0889-9746.
J. K. Vandiver. Damping parameters for flow-induced vibration. *Journal of fluids and structures*, 35:105–119, 2012.
H. Wang, D. Zhao, W. Yang, and G. Yu. Numerical investigation on flow-induced vibration of a triangular cylinder at a low reynolds number. *Fluid Dynamics Research*, 47(1):015501, 2014.
Q. Wang, L. Gan, S. Xu, and Y. Zhou. Vortex evolution in the near wake behind polygonal cylinders. *Experimental Thermal and Fluid Science*, 110:109940, 2020. ISSN 0894-1777.
R. Wang, Y. Bao, D. Zhou, H. Zhu, H. Ping, Z. Han, D. Serson, and H. Xu. Flow instabilities in the wake of a circular cylinder with parallel dual splitter plates attached. *Journal of Fluid Mechanics*, 874:299–338, 2019.

S. Wang, L. Zhu, X. Zhang, and G. He. Flow past two freely rotatable triangular cylinders in tandem arrangement. *Journal of Fluids Engineering*, 2011.
Z. Wang and Y. Zhou. Vortex-induced vibration characteristics of an elastic square cylinder on fixed supports. *Journal of Fluids Engineering*, 2005.
C. Williamson and R. Govardhan. Vortex-induced vibrations. *Annu. Rev. Fluid Mech.*, 36:413–455, 2004.
C. H. Williamson. Vortex dynamics in the cylinder wake. *Annual review of fluid mechanics*, 28(1):477–539, 1996.
F. Xie, Y. Yu, Y. Constantinides, M. S. Triantafyllou, and G. E. Karniadakis. U-shaped fairings suppress vortex-induced vibrations for cylinders in cross-flow. *Journal of Fluid Mechanics*, 782:300–332, 2015.
S. Xu, W. Zhang, L. Gan, M. Li, and Y. Zhou. Experimental study of flow around polygonal cylinders. *Journal of Fluid Mechanics*, 812:251–278, 2017.
X. Yang, Z. Yan, Y.-B. Yang, L. Wang, and S. Zhao. Study on the drag reduction and vortex-induced vibration of an 18-sided polygon cylinder. *Ocean Engineering*, 295:116961, 2024.
Y. Yu, F. Xie, H. Yan, Y. Constantinides, O. Oakley, and G. E. Karniadakis. Suppression of vortex-induced vibrations by fairings: a numerical study. *Journal of Fluids and Structures*, 54:679–700, 2015.
J. Zhang, G. Xu, F. Liu, J. Lian, and X. Yan. Experimental investigation on the flow induced vibration of an equilateral triangle prism in water. *Applied Ocean Research*, 61:92–100, 2016.
X. Zhang, D. Chen, Y. Luo, Y. Lin, J. Liu, and G. Pan. Vortex-induced vibration characteristics of rigidly connected four-cylinder system and nonlinear energy sinks for vibration suppression. *Physics of Fluids*, 36(6), 2024.
J. Zhao, J. S. Leontini, D. L. Jacono, and J. Sheridan. Fluid structure interaction of a square cylinder at different angles of attack. *Journal of Fluid Mechanics*, 747:688–721, 2014.
M. Zhao, L. Cheng, and T. Zhou. Numerical simulation of vortex-induced vibration of a square cylinder at a low reynolds number. *Physics of Fluids*, 25(2):023603, 2013.